Cloud liquid water path detectability and retrieval accuracy from airborne passive microwave observations over Arctic sea ice

Nils Risse[1], Mario Mech[1], Catherine Prigent[2], Joshua J. Müller[3], and Susanne Crewell[1]

[1]Institute for Geophysics and Meteorology, University of Cologne, Cologne, Germany
[2]Laboratoire d'Instrumentation et de Recherche en Astrophysique, Observatoire de Paris, CNRS, Paris, France
[3]Leipzig Institute for Meteorology, University of Leipzig, Leipzig, Germany

Correspondence: Nils Risse (n.risse@uni-koeln.de)

Abstract. Clouds are critical in the Arctic's water balance and energy budget. Especially, the cloud liquid water path (CLWP) modifies the cloud radiative properties and affects the surface energy balance. Spaceborne microwave radiometers provide a high sensitivity to CLWP at pan-Arctic scales, but extracting this information over sea ice requires separation of surface and cloud emission. Here, we assess CLWP detectability and retrieval accuracy over sea ice from a physical optimal estimation retrieval applied to airborne passive microwave observations during the HALO–$(\mathcal{AC})^3$ campaign. Reference data on surface temperature, young ice fraction, hydrometeor occurrence, and cloud liquid layers are available from collocated airborne instruments. The retrieval estimates CLWP and five surface parameters by inverting a forward operator consisting of the Snow Microwave Radiative Transfer (SMRT) and Passive and Active Microwave radiative TRAnsfer (PAMTRA) models. We find a consistent representation of sea ice and snow emission from 22–183 GHz under clear-sky conditions in both observation and state space. The CLWP detectability, defined as the 95th percentile of retrieved CLWP under clear-sky conditions, is about $50\,\mathrm{g\,m^{-2}}$ in the Central Arctic and increases towards the marginal ice zone up to $350\,\mathrm{g\,m^{-2}}$. The CLWP retrieval accuracy increases with increasing CLWP, with a relative root mean squared error below 50 % for CLWP above $100\,\mathrm{g\,m^{-2}}$. Retrieval uncertainties occur due to ambiguities between cloud liquid water emission and scattering in the snowpack and emission by newly formed sea ice. We further analyze the impact of surface melt and a rain-on-snow event associated with the warm air intrusion on the surface parameters. Finally, we show CLWP distributions along the flight track for all HAMP observations in comparison to ERA5 for different cloud regimes. The retrieval algorithm enhances the understanding of Arctic clouds and allows for an improved use of passive microwave satellite data in polar regions.

1 Introduction

The Arctic is warming at a faster rate than the global average in recent decades (Rantanen et al., 2022). Clouds play a critical role as a feedback mechanism in the amplified warming in the Arctic (Tan et al., 2021). Cloud liquid water modifies the cloud radiative effect (Shupe and Intrieri, 2004; Ebell et al., 2020) with implications for the surface energy budget (Sledd et al., 2025). Additionally, cloud liquid water plays a critical role in precipitation formation processes, such as efficient ice crystal growth through riming (Maherndl et al., 2024). Passive microwave radiometers allow for a quantification of the cloud liquid water path (CLWP), defined as the columnar integral of cloud liquid water content, by observing the temperature-dependent

microwave emission of liquid droplets (Kneifel et al., 2014; Turner et al., 2016). This emission of liquid droplets increases with frequency, and retrievals typically use observations at window channels in the range from 19 to 90 GHz (Greenwald et al., 1993; Crewell and Löhnert, 2003). Over sea ice, high-quality CLWP estimates are provided from ship-based microwave radiometers (Westwater et al., 2001; Walbröl et al., 2022). Operational satellite CLWP products are currently not available over sea ice due to the variable emission and polarization of the sea ice and snow. For example, the Multisensor Advanced Climatology of Liquid Water Path (MAC-LWP; Elsaesser et al., 2017; O'Dell et al., 2008) is limited to ice-free ocean, and the Microwave integrated Retrieval System (MiRS; Boukabara et al., 2011) provides estimates over ice-free ocean and land only. First estimates of the CLWP retrieval accuracy from passive microwaves are presented by Haggerty et al. (2002) using airborne microwave observations and collocated in situ data. Their results show a high accuracy for CLWP above $100\,\mathrm{g\,m^{-2}}$ and poor accuracy for CLWP below $50\,\mathrm{g\,m^{-2}}$. Generally, the CLWP uncertainty increases with increasing surface emissivity due to the decreasing contrast between the liquid cloud emission and the surface (Prigent et al., 2003). Hence, airborne or satellite retrievals of atmospheric properties require an accurate representation of the surface emissivity and its polarization.

Several methods were developed to describe the emissivity of sea ice and snow-covered surfaces. Emissivity atlases derived from long-term satellite observations under clear-sky with collocated surface temperature data provide robust first-guess emissivities and their variability (Prigent et al., 1997; Wang et al., 2017). However, as the emissivity variability over sea ice can be very high, the long-term mean might deviate ~~largely~~ significantly from the actual emissivity (Perro et al., 2020). To better capture this emissivity variability, dynamic emissivity modeling approaches are developed in a data assimilation context (e.g., Di Tomaso et al., 2013). This approach computes the emissivity at window channels and extrapolates to neighboring sounding channels in the same field-of-view, but is limited to clear-sky conditions. A novel machine learning approach by Geer (2024) addresses the need for better sea ice emissivity modeling in a numerical weather prediction context over sea ice (Lawrence et al., 2019). The approach exploits long-term observations to learn a compact representation of relevant sea ice and snow microphysical properties and their empirical transformation to an emissivity. While machine learning provides a computationally efficient approach, interpreting the underlying geophysical parameters is challenging. Physical snow and sea ice radiative transfer modeling approaches directly compute the emission from plane parallel sea ice and snow layers and their properties, such as density, grain size, salinity, temperature, thickness, and microstructure (Tonboe et al., 2006). The Arctic-wide retrieval by Rückert et al. (2023b) validated with observations from the Multidisciplinary drifting Observatory for the Study of Arctic Climate (MOSAiC) expedition provides simultaneous atmospheric and sea ice properties from an optimal estimation retrieval framework. While their retrieval used a fixed assumption on the snow and ice layering, Kang et al. (2023) explored the coupling of a sea ice and snow radiative transfer model with a thermodynamic sea ice and snow evolution model to better capture snow metamorphism and temporal variations in snow layering. This approach could be useful in a coupled land-atmosphere assimilation of surface-sensitive microwave channels (Hirahara et al., 2020). Yet, we lack a detailed assessment of the CLWP detectability and retrieval accuracy from passive microwave observations over sea ice.

To study the CLWP signal over sea ice, we develop an optimal estimation sea ice–atmosphere retrieval specifically for airborne passive microwave observations from 22–183 GHz at nadir. The underlying forward operator simulates the brightness temperature (T_b) at flight altitude from a loose coupling of the Snow Microwave Radiative Transfer (SMRT; Picard et al., 2018)

model with the Passive and Active Microwave radiative TRAnsfer (PAMTRA; Mech et al., 2020) tool via the spectral surface emissivity and effective temperature. This physical modeling approach allows a simultaneous retrieval of snow layer properties (correlation length and thickness), snow and sea ice temperature, and CLWP, under non-heavy cloud ice and snow conditions, since frozen water path is not retrieved. We apply the retrieval to the airborne Microwave Package (HAMP; Mech et al., 2014) radiometer onboard the *High Altitude and Long Range Research Aircraft* (*HALO*) during the HALO–$(\mathcal{AC})^3$ field campaign carried out in spring 2022 in the Fram Strait and Central Arctic. *HALO's* cloud observatory suite (Stevens et al., 2019) with coincident cloud radar, lidar, and infrared observations provides a unique opportunity for passive microwave retrieval evaluation (Jacob et al., 2019). We aim to (1) assess the representation of sea ice and snow microwave emission by the forward model, (2) estimate the CLWP detectability and retrieval accuracy, and (3) analyze the spatial variability of CLWP over sea ice during HALO–$(\mathcal{AC})^3$.

The paper is structured as follows. Section 2 provides an overview of the airborne field data and auxiliary satellite and reanalysis data. Section 3 describes the sea ice–atmosphere retrieval and the forward operator. Section 4 details the clear-sky evaluation (first objective), CLWP detectability, and CLWP retrieval accuracy (second objective). Section 5 addresses the third objective by presenting the retrieval application to two case studies, a rain-on-snow event, and comparing the CLWP from HAMP with ERA5. The study is summarized and concluded in Sect. 6.

2 Data

2.1 HALO–$(\mathcal{AC})^3$ field campaign

The multi-platform field campaign HALO–$(\mathcal{AC})^3$ included 17 flights with the research aircraft *HALO* between 11 March and 12 April 2022 over sea ice in the Fram Strait and Central Arctic (Wendisch et al., 2024; Ehrlich et al., 2024). Thus, *HALO* captured diverse sea ice conditions from young ice near the sea ice edge to perennial sea ice north of Greenland. Here, we include all observations over at least 90 % sea ice concentration (Spreen et al., 2008) with a distance of more than 15 km to coasts (Fig. 1). Due to the coarser spatial resolution of the sea ice product compared to the airborne observations, few open water pixels remain in the airborne data.

The meteorological conditions during HALO–$(\mathcal{AC})^3$ were dominated by warm air intrusions from 11–20 March 2022 and colder northerly winds from 21 March 2022 until the end of the campaign (Walbröl et al., 2024). The warm air intrusions caused rainfall on sea ice up to about 83° N (see Fig. 10 in Walbröl et al., 2024), which *HALO* captured on three consecutive days (11–13 March 2022).

The cloud observatory configuration of *HALO* includes a microwave radiometer, cloud radar, lidar, thermal infrared radiometer, thermal infrared spectral imager, and solar spectral imager. In addition, 85 dropsonde launches over sea ice provide vertical profiles of air temperature, humidity, and wind between flight altitude and the surface (George et al., 2024). This dropsonde data was partly assimilated into the European Centre for Medium-Range Weather Forecasts (ECMWF) Integrated Forecasting System (IFS). Details on the *HALO* instrumentation and dropsonde assimilation can be found in Ehrlich et al. (2024). An

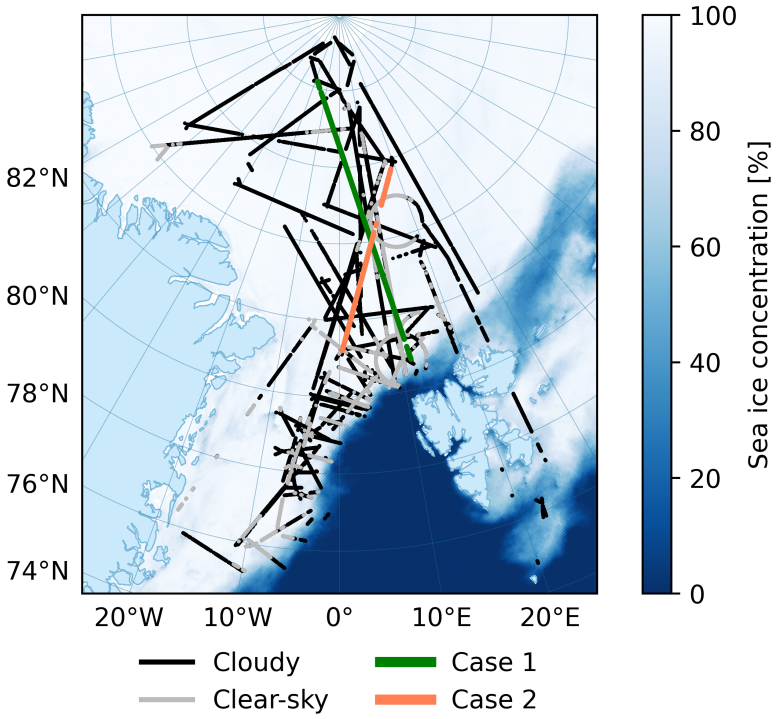

Figure 1. Map of the *HALO* flight track and mean sea ice concentration (Spreen et al., 2008). Only positions where the retrieval was applied are shown.

example of the microwave radiometer, radar, and lidar observations is provided in Fig. 2 for a 550 km southbound transect. The following sections describe the instruments and products of the cloud observatory configuration and ancillary products.

2.2 Microwave radiometer

The HAMP radiometer measures at 25 channels in the frequency range from 22.24 to 183.31±7.5 GHz (Mech et al., 2014). Six channels each are located along the 22.24 GHz water vapor absorption line and around the 183.31 GHz water vapor absorption line, seven channels are located along the 50–60 GHz oxygen absorption complex, four channels are located around the 118.75 GHz oxygen absorption line, and two channels are located within atmospheric windows at 31.4 and 90 GHz. HAMP points nadir and samples with a temporal resolution of 1 s. The footprint sizes range from about 0.7 to 1.4 km at typical *HALO* flight altitude and speed (Table 1). The data was corrected for biases using dropsondes over open ocean (Dorff et al., 2024). Here, we use an updated version of the bias correction. Measurement gaps that were filled by temporal interpolation in the published data are discarded, and we removed any observations where aircraft roll or pitch exceed ±6°. Moreover, we exclude about 19 % of the observations due to potentially high scattering by frozen hydrometeors or surface melt. In total, about 85,000

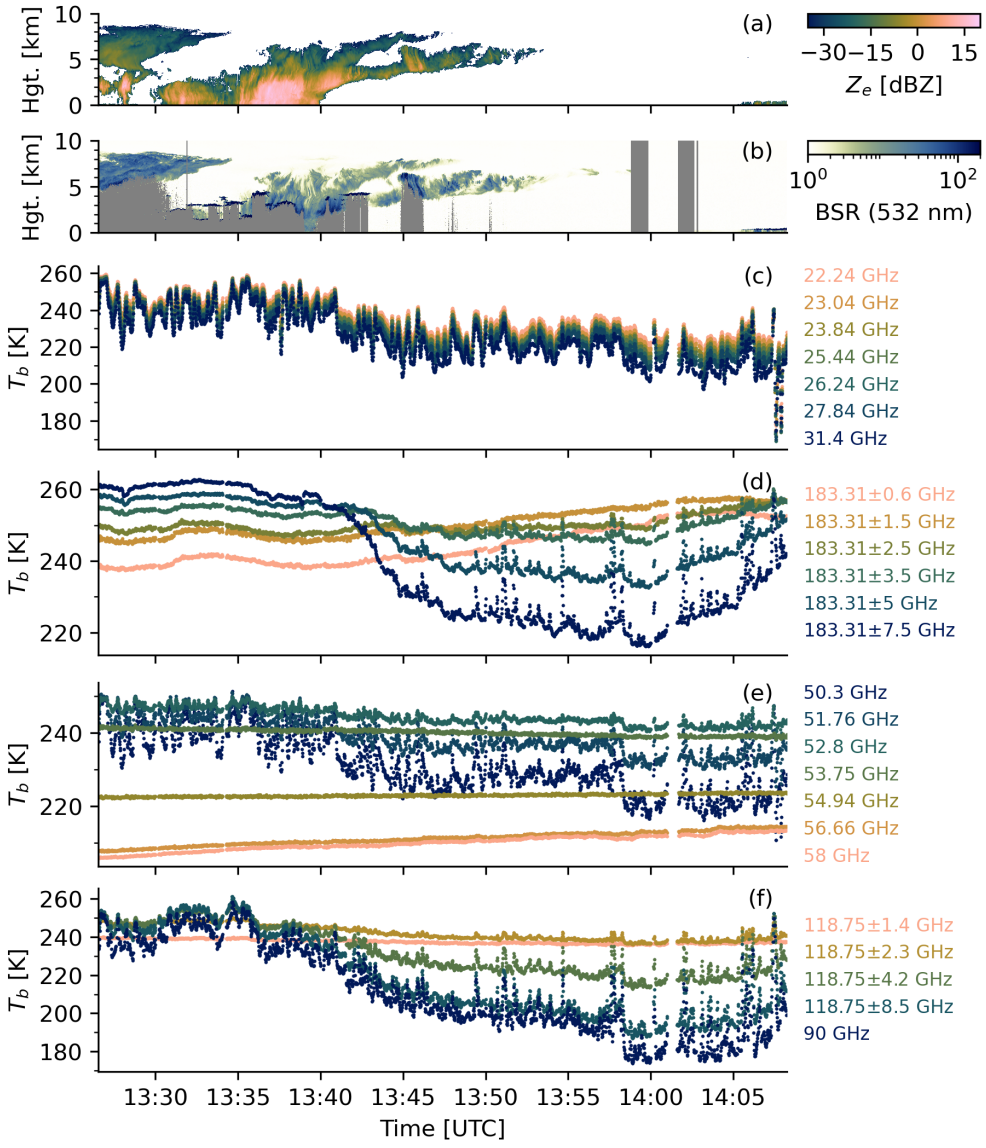

Figure 2. Radar, lidar, and microwave radiometer observations during a 550 km southbound transect over sea ice on 14 March 2022 (case 2 in Fig. 1). (a) Radar reflectivity, (b) lidar backscatter ratio, (c) T_b from 22 to 31 GHz, (d) T_b around 183.31 GHz, (e) T_b from 50 to 58 GHz, and (f) T_b at 90 and around 118.75 GHz. Missing/flagged data is shown in gray.

Table 1. Beam width, noise equivalent differential temperature (NeDT), and footprint size of HAMP channels. The footprint size is calculated for a flight velocity of 300 $\mathrm{m\,s^{-1}}$ and 12 km flight altitude.

Channels	Frequency range [GHz]	Beam width [°]	NeDT [K]	Footprint size [$\mathrm{km^2}$]
1–7	22.24–31.4	5	0.1	1.1×1.4
8-14	50.3–58	3.5	0.2	0.7×1
15	90	3.3	0.25	0.7×1
16–19	110.25–127.25	3.3	0.6	0.7×1
20–25	175.81–190.81	2.7	0.6	0.6×0.9

HAMP samples are available over sea ice along a flight distance of 20,000 km between -55–27° E and 74.8–89.4° N, out of which about 14 % (12,200) were clear-sky as identified from the radar–lidar cloud mask with available thermal infrared data.

Most weighting functions of HAMP peak at the surface under cold and dry Arctic conditions. Thus, the T_b varies due to changes in surface emission along the flight track with a high correlation between neighboring surface-sensitive channels (Fig. 2c–f). Therefore, we only use six HAMP channels for the retrieval: 22.24, 31.4, 50.3, 90, 118.75±8.5, and 183.31±7.5 GHz. This includes channels typically used for ground-based and satellite CLWP retrievals, with the highest sensitivity at 90 and 118.75±8.5 GHz. Moreover, these channels fully exploit HAMP's spectral range for surface characterization.

2.3 Radar–lidar cloud mask

The cloud radar and lidar onboard *HALO* provide reference data on the occurrence of hydrometeors in the field of view of HAMP. Especially, the lidar is highly sensitive to liquid cloud layers. Both instruments and derived products are described below.

The HAMP cloud radar operates in the Ka-band at 35.5 GHz with a temporal resolution of 1 s and vertical resolution of 30 m (Ewald et al., 2019). The sensitivity of the HAMP radar is about -30 dBZ (Konow et al., 2019). Here, we use the radar reflectivity product aligned temporally with the passive microwave radiometer observations and filtered for ground clutter in ~~the lowest about~~ approximately the lowest 100 m (Dorff et al., 2024). Hence, shallow fog layers cannot be detected by the radar. Compared to the microwave radiometer, the radar ~~'s footprint size is rather narrow, with about~~ has a rather small footprint size of approximately 130 m (Mech et al., 2014).

Backscatter lidar and water vapor differential absorption lidar profiles were measured by the airborne demonstrator for the WAter vapor Lidar Experiment in Space (WALES; Wirth et al., 2009). Here, we use the backscatter ratio (BSR) and depolarization ratio at 532 nm, which are available with a vertical resolution of 15 m and a temporal resolution of 1 s (Wirth and Groß, 2024). We exclude all data with a non-zero quality flag and below 50 m above the surface.

The radar observation is defined as cloudy if the radar reflectivity of any bin exceeds -40 dBZ. Similarly, we apply a backscatter ratio threshold of 4 to the lidar column. We define a scene as cloudy if either the radar or the lidar observations fulfill their cloud mask criterion. Both thresholds reduce the impact of thin ice clouds on the thermal infrared radiometer measurements.

In addition to the hydrometeor detection, we need to identify scenes with potential impact of scattering by frozen hydrometeors, which is relevant at HAMP frequencies above 90 GHz (Bennartz and Bauer, 2003). Here, we use a maximum radar reflectivity threshold of 5 dBZ at any height level in the radar column, which corresponds to a snowfall rate of about 0.05 to 0.5 $\mathrm{mm\,h^{-1}}$ depending on the ice particle habit and size distribution (Kneifel et al., 2011).

Further, we build a detection method for liquid cloud layers based on the lidar backscatter ratio and depolarization ratio. Cloud regions dominated by liquid water exhibit a high backscatter and near-zero depolarization ratio (Shupe, 2007; De Boer et al., 2009; Luke et al., 2010). Several threshold-based methods are developed for liquid classification from both parameters (Kalesse-Los et al., 2022), and here we subjectively define a similar thresholding method from the examination of WALES statistics of both parameters for HALO–$(\mathcal{AC})^3$. We define a region as liquid-dominated if the depolarization ratio is below 0.1 and the backscatter ratio is above 50. Typically, only the uppermost liquid layer can be detected from airborne lidars, and we define the uppermost bin of liquid-dominated regions as liquid layer top height (h_l). To account for attenuation of the lidar beam by large amounts of frozen hydrometeors, we classify columns that did not satisfy the liquid water criterion as potentially liquid clouds if the radar hydrometeor fraction in the lowest 5 km exceeds 50 $\%$.

2.4 Radiation data

The thermal infrared radiometer KT-19 provides T_b in the atmospheric window from 9.6–11.5 $\mu\mathrm{m}$ (Schäfer et al., 2022). The T_b accuracy of KT-19 is about 0.5 K. The instrument points nadir with a beam width of 2.3°, which is comparable to the HAMP radiometer channels. The sampling frequency of 20 Hz is averaged to 1 Hz to match the HAMP radiometer sampling. We convert the clear-sky infrared T_b to surface skin temperature under the assumption of an infrared emissivity of 0.995 (Høyer et al., 2017; Thielke et al., 2022). Remaining atmospheric effects in the atmospheric window are considered to be negligible. This data is used as a data source for the development of the microwave-only retrieval.

The Video airbornE Longwave Observations within siX channels (VELOX) camera provides two-dimensional thermal infrared T_b in the atmospheric window from 8.65–12 $\mu\mathrm{m}$ (Schäfer et al., 2022). The data are available at a temporal resolution of 1 s (Schäfer et al., 2023a). Here, we use the $10.74\pm0.39\,\mu\mathrm{m}$ channel (band 3) for qualitative information on spatial surface temperature features. From each image, we extract the cross-track scan at nadir. This data is used as a visualization during case studies.

The VELOX-based clear-sky surface classification product groups each pixel into four surface types, i.e., open water, sea ice water mixture, thin sea ice, and snow-covered sea ice (Müller et al., 2025b). The classification exploits spatial skin temperature variations of sea ice, snow, and open water with a spatial resolution of about $10\times10\,\mathrm{m}^2$. We derive the thin sea ice area fraction within the microwave radiometer footprint from the high-resolution pixel-based classification. The accuracy of the thin sea ice classification, defined as the ratio of correct to total predictions, is approximately 70 $\%$ (Müller et al., 2025b). We use this data for retrieval evaluation under clear-sky conditions.

The spectrometer of the Munich Aerosol Cloud Scanner (specMACS) measures two-dimensional fields of reflected spectral radiances from 0.4–2.5 µm (Ewald et al., 2016; Weber et al., 2024a). SpecMACS points nadir with a field of view of about 35° and a temporal resolution of 30 Hz. Since the visible bands were not available during HALO–$(\mathcal{AC})^3$, we use the 1 µm near infrared radiance for qualitative information on clouds and surface conditions. This data is used as a visualization during case studies.

2.5 Ancillary products

The ERA5 reanalysis provides hourly air temperature, pressure, and specific humidity on 137 model levels, and skin temperature, 2 m air temperature, and total column liquid water on surface levels at a spatial resolution of 31 km resampled to 0.25×0.25° (Hersbach et al., 2020). Here, we use data from the ERA5 grid cells that are nearest in space and time to the *HALO* flight track. The data is used as input for the retrieval and, in the case of the total column liquid water, for comparison with the CLWP retrieved from HAMP. The 2 m air temperature is used to filter potential surface melt, which occurred during parts of the warm air intrusion over sea ice. Here, we use a 2 m air temperature threshold of -1 °C.

Daily sea ice concentration maps from the University of Bremen with a 6.25×6.25 km^2 resolution based on Advanced Microwave Scanning Radiometer - 2 (AMSR2) 89 GHz observations (Spreen et al., 2008) are used to filter for observations over sea ice. To include data close to the north pole not covered by the AMSR2 swath, we assume sea ice concentrations are above 90 % in this area. Based on this data, we define the sea ice edge as the 50 % sea ice concentration contour and the Central Arctic as a region with a distance of at least 200 km from the sea ice edge. The number of samples with thin ice fraction above 25% is much lower in the Central Arctic (1%) compared to all observations (20%) based on the clear-sky VELOX estimate.

We use Level 1C T_b data from channel 17 of the Special Sensor Microwave Imager/Sounder (SSMIS; Kunkee et al., 2008) onboard the DMSP-F16 satellite to get qualitative information on the spatial T_b variability around the *HALO* track (NASA Goddard Space Flight Center and GPM Intercalibration Working Group, 2022). Channel 17 of SSMIS measures vertically polarized T_b at 91 GHz under an incidence angle of 53° with a footprint size of 9×15 km^2.

3 Sea ice–atmosphere retrieval

3.1 Retrieval overview

For a coupled sea ice–atmosphere retrieval using a physical forward operator, we need to solve the radiative transfer of both the cryosphere and the atmosphere. Unfortunately, no model exists that simultaneously solves the radiative transfer equations of both spheres. Therefore, previous work on sea ice–atmosphere retrievals performed a loose coupling between the sea ice and snow radiative transfer model and radiative transfer model for the atmosphere via T_b or emissivity and emitting layer temperature (e.g., Kang et al., 2023; Sandells et al., 2024). Here, we follow the same approach and loosely couple the radiative transfer models SMRT (Picard et al., 2018) for the surface and PAMTRA (Mech et al., 2020) for the atmosphere. Both models

are called sequentially, and the surface radiative properties are provided to PAMTRA as frequency-dependent emissivity and emitting layer temperature. This workflow is depicted in Fig. 3a and relevant input parameters are listed in Table 2.

Using optimal estimation (Rodgers, 2000), we retrieve six state parameters from the HAMP observations, considering observation, forward model, and a priori uncertainties. The retrieved state parameters are CLWP and five surface parameters: wind slab correlation length, depth hoar correlation length, wind slab thickness, snow–ice interface temperature, and air–snow interface temperature. The selection of these state parameters is based mainly on two criteria. First, there should be high sensitivity to state parameter variations within the parameter uncertainty range at HAMP frequencies based on SMRT–PAMTRA simulations. Second, ambiguities in the radiometric sensitivity between state parameters should be minimized to ensure stable retrieval convergence, i.e., correlations between columns of the Jacobian should be low. Note that CLWP is the only atmospheric parameter that gets retrieved. The selection of snow parameters is also motivated by Wivell et al. (2023), who found that varying wind slab correlation length, depth hoar correlation length, and wind slab thickness reproduces observed tundra snow emissivity spectra from 89 to 243 GHz.

The other two parameter groups are model parameters and fixed parameters. Unlike the state parameters, these two are not optimized during the retrieval. The model parameters are used to estimate the uncertainty of the forward model by varying them within a realistic range. The fixed parameters are estimated to have the lowest impact on the radiative transfer simulations and are sufficiently well known at the observation location. Therefore, these parameters are kept constant during the optimization.

The simulated radiometric signatures of state and model parameters at HAMP channels are presented in Fig 4. CLWP mainly affects the high-frequency channels at 90 and 118 GHz, similar to the wind slab correlation length and density. Increments in the wind slab thickness mainly affect the 50 and 90 GHz channels. Changes in depth hoar correlation length, thickness, and density mostly affect the observations from 22–51 GHz. The air–snow interface temperature mostly influences the high-frequency channels (90–183 GHz), while the snow–ice interface temperature influences the 22–31 GHz channels. Increments in the specularity parameter mainly affect channels with higher atmospheric optical depth, i.e., at 50, 118, and 183 GHz.

The main challenge for the retrieval is the lack of ground truth on the surface characteristics along the flight track. Therefore, we define two retrievals, hereafter referred to as retrieval 1 (R1; Fig. 3b) and retrieval 2 (R2; Fig. 3c). R1 is only applied to clear-sky and retrieves four surface parameters using wind slab and depth hoar correlation length a priori from the literature and an a priori guess of the wind slab thickness. Additionally, the air–snow interface is taken from KT-19, and CLWP is fixed to $0\,\mathrm{g\,m^{-2}}$. The retrieved distribution for all clear-sky samples (mean and standard deviation) of wind slab correlation length, depth hoar correlation length, and wind slab thickness is then used as a priori for the microwave-only retrieval R2 for both clear-sky and cloudy conditions to remove potential biases of the a priori values in R1. The clear-sky data used for the calibration covers most parts of the *HALO* study area and is therefore likely representative for cloudy scenes (Fig. 1).

3.2 ~~Optimal estimation~~

During the optimal estimation retrieval, the state vector $\boldsymbol{x}$ is iteratively updated until an optimal solution is found. Here, we use a priori as a first guess. The updated state

$$\boldsymbol{x_{i+1}} = \boldsymbol{x_a} + \mathbf{S_i}\mathbf{K_i}^T\mathbf{S_e}^{-1}[(\boldsymbol{y} - F(\boldsymbol{x_i}, \boldsymbol{b}) + \mathbf{K_i}(\boldsymbol{x_i} - \boldsymbol{x_a})]$$

is computed from the observation $\boldsymbol{y}$ (HAMP T_b), effective measurement uncertainty $\mathbf{S_e}$, a priori state $\boldsymbol{x_a}$, forward operator F, forward model parameters $\boldsymbol{b}$, Jacobian matrix $\mathbf{K_i}$ of the forward operator $F(\boldsymbol{x_i}, \boldsymbol{b})$, and retrieval uncertainty $\mathbf{S_i}$. The effective measurement uncertainty combines observation and model uncertainty, i.e.,

$$\mathbf{S_e} = \mathbf{S_y} + \mathbf{K_b}\mathbf{S_b}\mathbf{K_b}^T,$$

with the observation uncertainty $\mathbf{S_y}$, the Jacobian matrix for model parameters $\mathbf{K_b}$ (computed during each iteration), and the model parameter uncertainty $\mathbf{S_b}$. We choose an uncorrelated observation uncertainty of 1.5 from 22 to 118 GHz and 2 at 183 GHz. Table 2 lists the mean and uncertainty of the model parameters (wind slab density, depth hoar density, depth hoar thickness, and specularity).

The retrieval uncertainty is given as

$$\mathbf{S_i} = (\mathbf{S_a}^{-1} + \mathbf{K_i}^T\mathbf{S_e}^{-1}\mathbf{K_i})^{-1},$$

with the a priori covariance matrix $\mathbf{S_a}$. The optimal solution and its a posteriori uncertainty are found if the condition

$$(\boldsymbol{x_i} - \boldsymbol{x_{i+1}})^T\mathbf{S_i}^{-1}(\boldsymbol{x_i} - \boldsymbol{x_{i+1}}) < \frac{N}{10}$$

is met within six iterations. The retrieval algorithm assumes that the parameters follow a Gaussian distribution. While this is valid for most parameters, the CLWP may differ from a Gaussian distribution. A logarithmic transformation of CLWP similar to Boukabara et al. (2011) will be applied in the future.

Flow diagrams of the (a) SMRT–PAMTRA forward operator ($F(x,b)$) coupled via emissivity (e) and effective temperature (T_{eff}), (b) clear-sky retrieval to calibrate snow parameters (R1), and (c) retrieval for clear-sky and cloudy conditions (R2). The parameter labeling of the forward operator in (a) corresponds to the retrieval for clear-sky and cloudy conditions in (c) (the air–snow interface temperature (T_{as}) and cloud liquid water path ($CLWP$) are fixed parameters in (b)). Note that the surface is characterized by fractions of young ice (YI) and multiyear ice (MYI), such that $f_{YI} + f_{MYI} = 1$. Parameter names of each symbol are listed in Table 2.

3.2 Optimal estimation

During the optimal estimation retrieval (Rodgers, 2000), the state vector $\boldsymbol{x}$ is iteratively updated until an optimal solution is found. Here, we use a priori as a first guess. The updated state

$$\boldsymbol{x_{i+1}} = \boldsymbol{x_a} + \mathbf{S_i}\mathbf{K_i}^T\mathbf{S_e}^{-1}[(\boldsymbol{y} - F(\boldsymbol{x_i}, \boldsymbol{b}) + \mathbf{K_i}(\boldsymbol{x_i} - \boldsymbol{x_a})] \quad (1)$$

Table 2. State, model, and fixed parameters of the retrieval with references. The mean value of the state parameters denotes the a priori mean, while they denote the value used during the forward simulation for the model and fixed parameters. ERA5 or KT-19 mean values are derived from spatially and temporally collocated data. The standard deviation (Std.) denotes the square root of the diagonal of the a priori or model parameter covariance matrices. The minimum (Min.) and maximum (Max.) values indicate parameter limits.

Type	Parameter	Symbol	Unit	Mean	Std.	Min.	Max.	Reference
State	Cloud liquid water path	$CLWP$	$\mathrm{g\,m^{-2}}$	0^b	150	0	1000	
	Wind slab corr. length	ξ_{WS}	mm	0.13 0.12^a	0.05 0.03^a	0.05	0.25	Rückert et al. (2023b)
	Depth hoar corr. length	ξ_{DH}	mm	0.22 0.34^a	0.1 0.09^a	0.1	0.6	Rückert et al. (2023b)
	Wind slab thickness	h_{WS}	cm	~~13~~ 20 ~~12~~20^a	5 ~~3~~4^a	3	40	
	Snow–ice interface temp.	T_{si}	K	KT-19 ERA5	3	243.15	271.15	Schäfer et al. (2024) Hersbach et al. (2020)
	Air–snow interface temp.	T_{as}	K	KT-19^b ERA5	3	233.15	273.14	Schäfer et al. (2024) Hersbach et al. (2020)
Model	Wind slab density	ρ_{WS}	$\mathrm{kg\,m^{-3}}$	350	30	150	450	King et al. (2020)
	Depth hoar density	ρ_{DH}	$\mathrm{kg\,m^{-3}}$	200	30	100	400	Domine et al. (2007)
	Depth hoar thickness	h_{DH}	cm	15	3	3	40	
	Specularity	s	-	0	0.25	0	1	Guedj et al. (2010)
Fixed	Young ice fraction	f_{YI}	-	0				
	Air temperature	T_a	K	ERA5				Hersbach et al. (2020)
	Specific humidity	q_v	$\mathrm{kg\,kg^{-1}}$	ERA5				Hersbach et al. (2020)
	Multiyear ice density	ρ_{MYI}	$\mathrm{kg\,m^{-3}}$	850				Timco and Frederking (1996)
	Young ice density	ρ_{YI}	$\mathrm{kg\,m^{-3}}$	915				Timco and Frederking (1996)
	Multiyear ice corr. length	ξ_{MYI}	mm	0.28				Rostosky et al. (2020)
	Young ice corr. length	ξ_{YI}	mm	0.15				Rostosky et al. (2020)
	Multiyear ice thickness	h_{MYI}	cm	150				
	Young ice thickness	h_{YI}	cm	30				
	Multiyear ice salinity	S_{MYI}	psu	1.2				Cox and Weeks (1974)
	Young ice salinity	S_{YI}	psu	30				

[a] Determined from the clear-sky retrieval (Fig. 3b). [b] Fixed during the clear-sky retrieval (Fig. 3b)

is computed from the observation $\boldsymbol{y}$ (HAMP T_b), effective measurement uncertainty $\mathbf{S_e}$, a priori state $\boldsymbol{x_a}$, forward operator F, forward model parameters $\boldsymbol{b}$, Jacobian matrix $\mathbf{K_i}$ of the forward operator $F(\boldsymbol{x_i}, \boldsymbol{b})$, and retrieval uncertainty $\mathbf{S_i}$. The effective

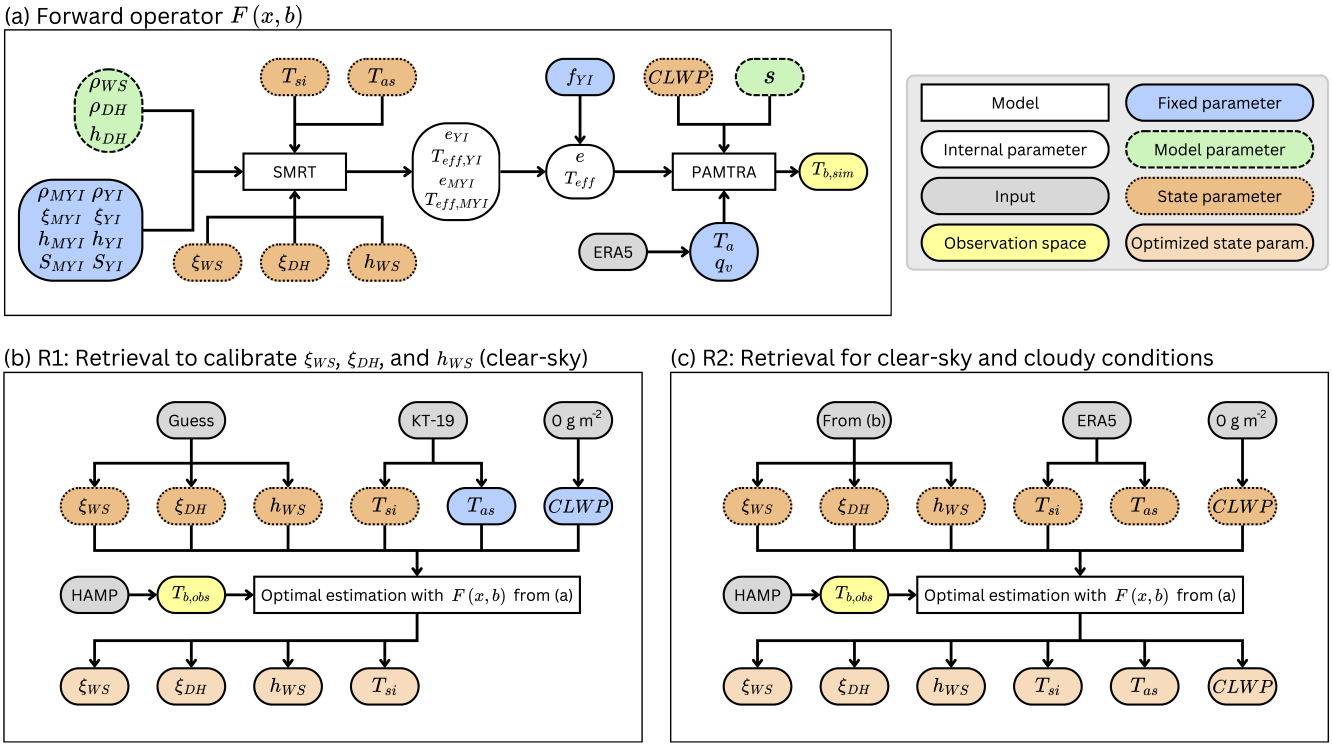

Figure 3. Flow diagrams of the (a) SMRT–PAMTRA forward operator ($F(x,b)$) coupled via emissivity (e) and effective temperature (T_{eff}), (b) clear-sky retrieval to calibrate snow parameters (R1), and (c) retrieval for clear-sky and cloudy conditions (R2). The parameter labeling of the forward operator in (a) corresponds to the retrieval for clear-sky and cloudy conditions in (c) (the air–snow interface temperature (T_{as}) and cloud liquid water path ($CLWP$) are fixed parameters in (b)). Note that the surface is characterized by fractions of young ice (YI) and multiyear ice (MYI), such that $f_{YI} + f_{MYI} = 1$. Parameter names of each symbol are listed in Table 2.

measurement uncertainty combines observation and model uncertainty, i.e.,

$$\mathbf{S_e} = \mathbf{S_y} + \mathbf{K_b}\mathbf{S_b}{\mathbf{K_b}}^T, \tag{2}$$

with the observation uncertainty $\mathbf{S_y}$, the Jacobian matrix for model parameters $\mathbf{K_b}$ (computed during each iteration), and the model parameter uncertainty $\mathbf{S_b}$. We choose an uncorrelated observation uncertainty of 1.5 K from 22 to 118 GHz and 2 K at 183 GHz. Table 2 lists the mean and uncertainty of the model parameters (wind slab density, depth hoar density, depth hoar thickness, and specularity).

The retrieval uncertainty is given as

$$\mathbf{S_i} = ({\mathbf{S_a}}^{-1} + {\mathbf{K_i}}^T{\mathbf{S_e}}^{-1}\mathbf{K_i})^{-1}, \tag{3}$$

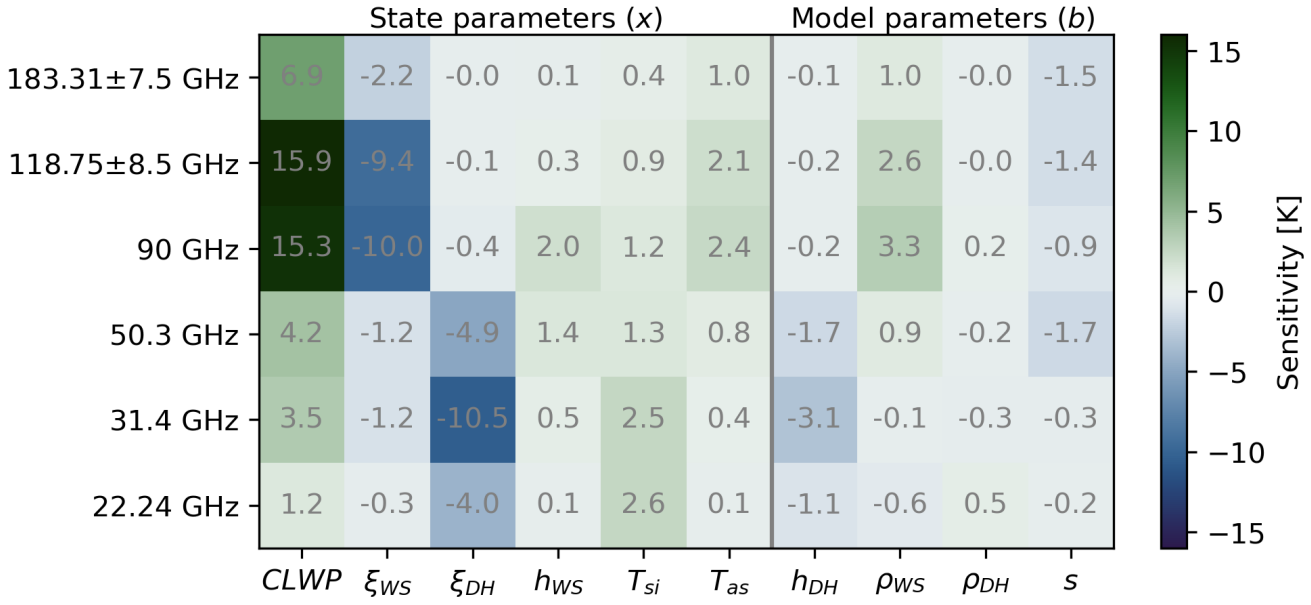

Figure 4. Simulated sensitivity of HAMP channels to variations in the state and model parameters during HALO–$(\mathcal{AC})^3$. The sensitivity is scaled by the standard deviation of each parameter in R2 (Table 2).

with the a priori covariance matrix $\mathbf{S_a}$. The optimal solution and its a posteriori uncertainty are found if the condition

$$(\boldsymbol{x_i} - \boldsymbol{x_{i+1}})^T \mathbf{S_i}^{-1} (\boldsymbol{x_i} - \boldsymbol{x_{i+1}}) < \frac{N}{10} \tag{4}$$

is met within six iterations, with the number of state parameters N. The retrieval algorithm assumes that the parameters follow a Gaussian distribution. While this is valid for most parameters, the CLWP may differ from a Gaussian distribution. A logarithmic transformation of CLWP similar to Boukabara et al. (2011) will be applied in the future.

3.3 Sea ice radiative transfer

The sea ice radiative transfer is solved with SMRT (Picard et al., 2018). SMRT simulates the microwave emission and scattering of horizontal and plane-parallel snow and sea ice layers. We assume that the snow consists of a mixture of ice and air without any liquid water or brine. Although liquid water likely occurred in the snowpack during parts of HALO–$(\mathcal{AC})^3$, a CLWP retrieval would be very uncertain over the highly emissive wet snow (Prigent et al., 2003; Vuyovich et al., 2017). The sea ice is characterized either as first-year or multiyear ice in SMRT. First-year ice comprises pure ice with brine inclusions, and multiyear ice comprises pure ice with brine and air inclusions. Below the sea ice, we add a semi-infinite ocean layer.

The propagation and scattering of microwave radiation in sea ice and snow depend on the snow and ice microstructure (Mätzler, 2002). Here, we use the exponential autocorrelation function as microstructure representation for both snow and sea ice, which is a function of the correlation length (Wiesmann et al., 1998). We select the improved Born approximation

as electromagnetic theory to compute the scattering coefficient, which was shown to reproduce observed T_b over snow from 5–243 GHz (Vargel et al., 2020; Sandells et al., 2022, 2024), and the discrete ordinate and eigenvalue radiative transfer solver (Picard et al., 2013). The permittivity of multiyear ice is calculated with the Polder–Van Santen mixing formulas. Spherical inclusions are assumed for brine in first-year ice and air bubbles in multiyear ice.

As we lack detailed sea ice and snow layer properties along the *HALO* flight track, we define two simplified sea ice types: snow-covered sea ice and bare young sea ice. The snow-covered sea ice comprises multiyear sea ice covered with a two-layer snowpack. Snow-covered first-year ice is not defined explicitly due to the limited sensitivity of frequencies above 18 GHz to the sea ice type with constant snow parameters based on SMRT (Soriot et al., 2022). The two-layer snow consists of a depth hoar and a wind slab layer, commonly observed in the Arctic (Merkouriadi et al., 2017; King et al., 2020). Wind slab typically consists of rounded snow grains, and its density is higher than the density of the underlying depth hoar. We do not retrieve the snow density, due to the limited sensitivity at the low HAMP frequencies and similar sensitivity to correlation length at high frequencies (Wivell et al., 2023). The snow thickness is set to ~~38~~35 cm a priori typical for the study region in spring (Warren et al., 1999) with a depth hoar fraction of about 40 % similar to field observations (King et al., 2020). The young sea ice is simulated as bare first-year sea ice, typically present in refrozen leads that are resolved by high-resolution aircraft observations and have a higher emissivity and surface temperature than surrounding sea ice (e.g., Hewison and English, 1999; Risse et al., 2024). Note that the young sea ice fraction is included in the forward operator for sensitivity tests only and not retrieved due to poor retrieval regulation when the influence of snow parameters decreases with increasing young ice fraction and the lack of accurate a priori data under cloudy conditions. Since the sea ice type and its physical properties do not notably impact the T_b at HAMP frequencies (Soriot et al., 2022), we can define a single-layer sea ice with fixed thickness, density, correlation length, and salinity (Table 2).

The sea ice and snow layer temperatures are linearly interpolated between the air–snow and snow–ice interface temperatures. An exception is the multiyear sea ice layer, where the snow–ice interface temperature is used as layer temperature, because the radiation emanates mostly from the upper part of the sea ice. Details on the a priori estimation are provided in Appendix B.

The emissivity (e) for each sea ice type (young ice or multiyear ice) is calculated using SMRT simulations of the upwelling brightness temperature ($T_{\mathrm{b,up}}$) with and without atmospheric downwelling brightness temperature ($T_{\mathrm{b,down}}$) following Wiesmann and Mätzler (1999), i.e.,

$$e = 1 - \frac{T_{\mathrm{b,up}}(T_{\mathrm{b,down}} = 100\,\mathrm{K}) - T_{\mathrm{b,up}}(T_{\mathrm{b,down}} = 0\,\mathrm{K})}{100\,\mathrm{K}}. \tag{5}$$

Then, the emitting layer or effective temperature (T_{eff}) is calculated as

$$T_{\mathrm{eff}} = \frac{T_{\mathrm{b,up}}(T_{\mathrm{b,down}} = 0\,\mathrm{K})}{e}. \tag{6}$$

The emissivity and effective temperature of the two sea ice types are combined using the young ice fraction. To reduce computational cost, we simulate e and T_{eff} only for the center frequencies of each channel and interpolate linearly to all HAMP band passes.

3.4 Atmospheric radiative transfer

The atmospheric radiative transfer is simulated with PAMTRA (Mech et al., 2020). PAMTRA computes the nadir T_b at the six HAMP channels for the flight altitude of *HALO*, considering the atmospheric and surface contributions. For the surface, we provide PAMTRA with the frequency-dependent emissivity and effective temperature simulated with SMRT. The Lambertian and specular contributions to surface reflection are weighted by specularity (s), where $s = 0$ ($s = 1$) corresponds to a fully Lambertian (specular) surface. The specularity parameter is set to 0 as found for winter over snow (Guedj et al., 2010; Harlow and Essery, 2012), with an uncertainty accounting for 25 % specular contribution. Atmospheric profiles are used from ERA5 and not adjusted during the retrieval (Appendix A). The gas absorption model by Rosenkranz (1998) is used with modifications of the water vapor continuum absorption (Turner et al., 2009).

The a priori CLWP is set to $0\,\mathrm{g\,m^{-2}}$ with a standard deviation of $150\,\mathrm{g\,m^{-2}}$. Although CLWP is available from ERA5, we keep the retrieval simple and always assume cloud-free conditions a priori. Negative CLWP values are set to $0\,\mathrm{g\,m^{-2}}$ before calling the forward operator. The CLWP is distributed with a homogeneous cloud liquid water content between the surface and 4 km height where the air temperature is above -38 °C and simulated using a monodisperse size distribution of 20 µm diameter. Both assumptions are considered to have a minimal impact on the simulated T_b (Crewell et al., 2009; Ebell et al., 2017). The emission of supercooled liquid water is derived following the model by Turner et al. (2016). Rain is not included in the forward simulations because we also do not consider associated wetting of the snowpack in our SMRT setup.

Cloud ice is not included in the simulation due to the low scattering at HAMP frequencies up to 183 GHz (e.g., Buehler et al., 2007). However, high amounts of larger snow particles lead to notable scattering from 90 to 183 GHz. For example, we observed T_b depressions up to 10 K at 183±7.5 GHz during parts of the warm air intrusion over sea ice during HALO–$(\mathcal{AC})^3$. However, since we remove these cases based on the radar reflectivity threshold, we assume that the remaining snow scattering can be neglected. Adding snow water path is in principle possible, but for simplicity, we focus on the cloud liquid water signal in this work.

3.5 Synthetic retrieval setup

The synthetic retrieval allows for the quantification of the CLWP retrieval accuracy and the identification of parameter ambiguities. The observation for the synthetic retrieval consists of realistic forward simulations of a known state rather than real observations. To create realistic forward simulations that resemble natural variability, we randomly generate state and model parameters using the a priori and model parameter covariance matrices. No noise is added to the synthetic forward simulations, but it is part of the effective measurement uncertainty of the retrieval. The synthetic database is built from random samples of HAMP observation positions and respective state, model, and fixed parameters to represent HALO–$(\mathcal{AC})^3$ conditions. The mean ERA5 integrated water vapor of the database is $5\,\mathrm{kg\,m^{-2}}$ with a standard deviation of $3\,\mathrm{kg\,m^{-2}}$, and the mean ERA5 skin temperature is -14 °C with a standard deviation of 8 K. For the CLWP accuracy assessment, we sample CLWP uniformly from 0–500 $\mathrm{g\,m^{-2}}$ and run 5000 simulations. For the identification of parameter ambiguities (2000 simulations), all parameters are sampled from Gaussian distributions truncated by the parameter limits (Table 2).

4 Retrieval evaluation

4.1 Clear-sky evaluation

4.1.1 Observation space

A comparison between the HAMP observation and simulations under clear-sky conditions (12,250 samples) provides an indication of whether the SMRT–PAMTRA forward operator represents real sea ice and snow conditions. In the following, we present T_b departure statistics of the a priori and optimal states for the retrievals R1 and R2 (Fig. 5). To ensure equal sampling, we analyze 81 % of the clear-sky observations where both R1 and R2 converge. Generally, R1 shows a slightly higher convergence rate with 90 % than R2 (87 %), which is expected due to the higher number of state parameters in R2.

The departures of the optimal solution improve notably and are much narrower than the a priori for both R1 and R2, especially from 22–118 GHz. The highest difference between the R1 and R2 distributions occurs at 90 and 118 GHz. While R1 tends to underestimate the T_b, R2 slightly overestimates the T_b in some cases by up to 10 K. For cases with T_b underestimation in R1, the R2 retrieval falsely adds CLWP. These cases occur mainly over young sea ice as identified from VELOX and are almost absent in the Central Arctic (not shown). The T_b overestimation of R2 is related to lower wind slab correlation lengths and also occurs during synthetic retrieval experiments, which might indicate instability due to the increased number of state parameters. Still, both distributions align ~~well~~ mostly with the effective measurement uncertainty despite the increase in state parameters from four to six from R1 to R2. The highest bias in R2 occurs at 22 GHz with -3 K~~, but the effect on the CLWP retrieval is expected to be small~~. This bias is primarily related to the presence of young ice, which reduces the T_b at 22 GHz. The biases of the other channels are much smaller (-0.6–1.5 K). This indicates a substantial improvement compared to the a priori with biases between -11 K at 22 GHz and 2 K at 118 GHz. A T_b bias correction could be performed at a later stage, but is not included here. The root mean squared error of the R2 retrieval varies between 2–4 K and lies close to the effective measurement uncertainty. Also, the correlations between observed and simulated T_b of the optimal solution are very high from 31–118 GHz with 0.9–0.93. ~~Hence,~~ Moreover, Appendix C shows similar inter-channel correlations between the observations and simulations under clear-sky conditions, except for an overestimation of the correlation between 22 and 183 GHz (Fig. C1). Overall, this clear-sky evaluation shows that the retrieval finds a state that ~~closely~~ mostly matches the observations, which provides the basis for the retrieval application to synthetic and cloudy observations.

4.1.2 State space

Encouraged by the good match of the retrieval with HAMP in observation space, we now analyze the corresponding retrieved state parameters (Fig. 6). The mean and standard deviation of the retrieved states in R1 for all clear-sky observations lie mostly close to the a priori mean and standard deviation. The largest difference occurs for the mean depth hoar correlation length, which increases by about 1.2σ (a priori uncertainty) from the a priori to the optimal state. This increase might be related to snow metamorphism throughout the winter, which increased depth hoar grain size and microwave scattering in this layer. This increase in a priori depth hoar correlation length explains the differences in the a priori T_b bias between R1 and R2 (Fig. 5). The

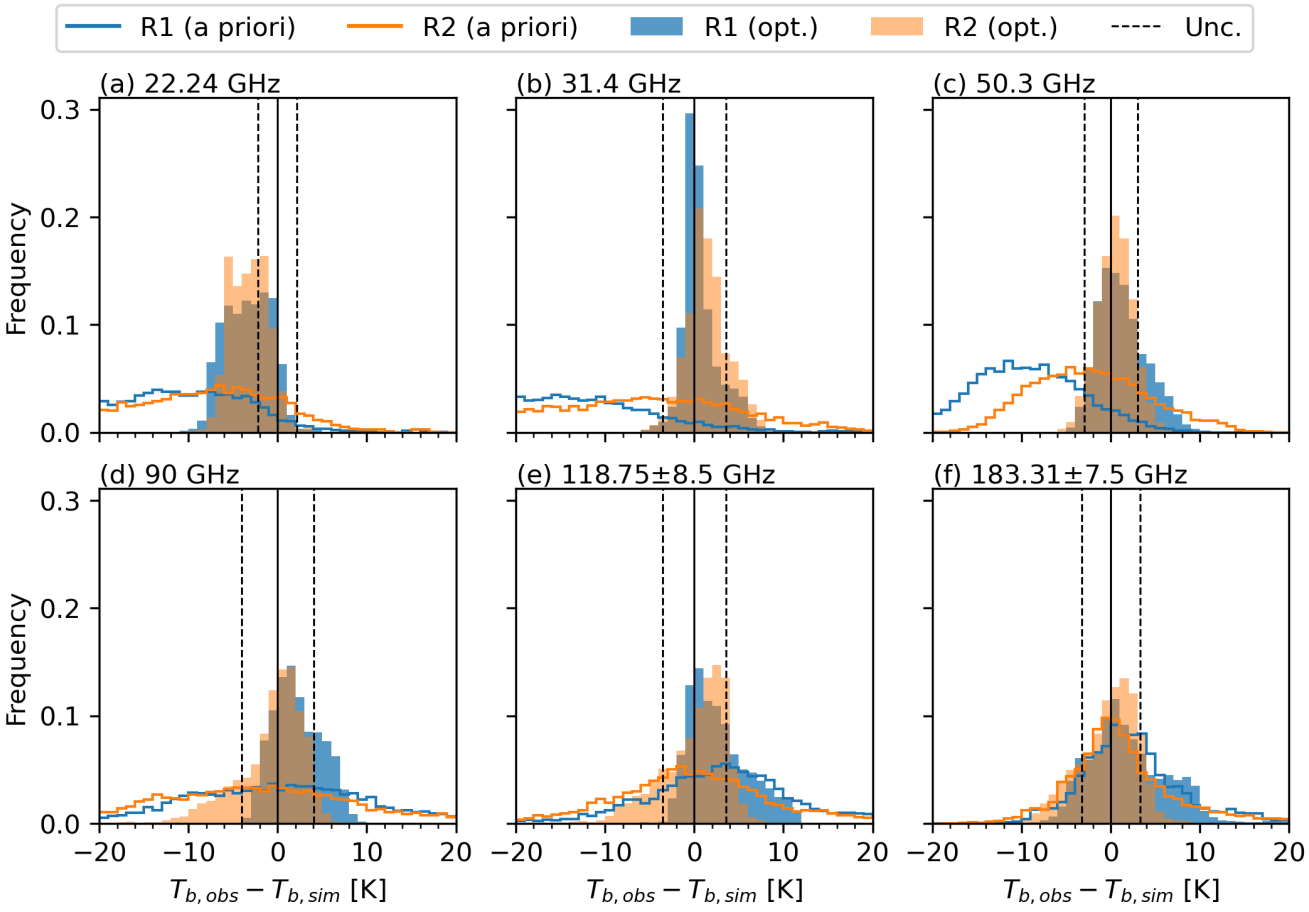

Figure 5. Histograms of the T_b departure between clear-sky observations and forward simulations of the a priori and optimal (opt.) states retrieved with R1 and R2. Panels show the (a) 22, (b) 31, (c) 50, (d) 90, (e) 118, and (f) 183 GHz channels. Note that only times where both retrievals converge are shown (81 % of the data). Unc.: Effective measurement uncertainty.

370 changes in the wind slab correlation length (-0.2σ) and wind slab thickness (0.2σ) are much smaller. The retrieved variability of the wind slab correlation length is lower than the value from the literature. For the snow–ice interface temperature, a relatively large negative deviation can be seen. This might be related to the observed negative bias of the a priori at low frequencies in Fig. 5 and might originate from the assumed relationship in Eq. (B1) or a misrepresentation of sea ice and snow layering. An assessment of the spatial consistency of these parameters is presented during the retrieval application in Sect. 5.

375 The distributions of the optimal parameters from the R2 retrieval shift slightly compared to the R1 retrieval, but differences are overall small (Fig. 6). This shows that the retrieved state is not very sensitive to the a priori mean, which is important for the poorly constrained snow parameters. Compared to R1, the R2 retrieval also derives the air–snow interface temperature, as this information will not be available under cloudy conditions. The retrieved temperature centers well around the ERA5-based

a priori estimate, indicating that the ERA5 skin temperature is a suitable a priori choice. The root mean squared error between the retrieved air–snow interface temperature and the skin temperature from KT-19 is 2.8 K, which is similar to the ERA5-based a priori (3.1 K; not shown). For CLWP, which is also retrieved by R2 and should ideally be zero under clear-sky identified from the radar–lidar cloud mask, the root mean squared error is 112 $\mathrm{g\,m^{-2}}$ (Fig. 6f). Generally, the state distributions are realistic despite some deviations in the snow–ice interface temperature, which affect the low-frequency HAMP channels. Thus, we conclude that the retrieval with the SMRT–PAMTRA forward operator provides a generalized representation of the sea ice and snow layer properties for a CLWP retrieval.

4.2 Cloud liquid water path detectability

This section analyses the CLWP detectability of the HAMP retrieval from clear-sky observations. During clear-sky conditions, the retrieved CLWP should ideally be close to 0 $\mathrm{g\,m^{-2}}$. Hence, we can define the CLWP detectability as the 95th percentile of retrieved CLWP under clear-sky (Fig. 7a). For all observations, about 95 % of the retrieved CLWP are below 306 $\mathrm{g\,m^{-2}}$. We identify a distinct spatial pattern in the Central Arctic (29% of clear-sky samples), where this detectability improves a lot down to 45 $\mathrm{g\,m^{-2}}$. This decrease with increasing distance to the ice edge is shown in Fig. 7b. Between 150–200 km, the detectability decreases from 300 to below 100 $\mathrm{g\,m^{-2}}$ and remains low for further distances to the ice edge. The infrared-based analysis by Müller et al. (2025b) shows a consistent decrease of refrozen leads with distance to the ice edge. These leads and their ~~respective~~ high microwave emissivity (e.g., Hewison and English, 1999) and skin temperature ~~are correlated~~ often align with false CLWP detections, with a correlation of 0.51 (Fig. 7c). ~~The high false detection for~~ For high thin ice fractions, almost all HAMP retrievals show falsely detected CLWP. False detections over low thin ice ~~fraction likely corresponds to thicker young ice, potentially with a snow cover, and a skin temperature comparable to surrounding sea ice~~ fractions likely correspond to observations over thicker and snow-covered young ice that are not identified by the thin ice detection algorithm. A similar T_b response between CLWP and increased bare ice fraction can also be simulated with SMRT and PAMTRA (Fig. 7d). Overall, the clear-sky retrieval evaluation shows that the retrieval detects CLWP above 50 $\mathrm{g\,m^{-2}}$ at higher distances from the ice edge and can thus be applied to cloudy scenes.

4.3 Cloud liquid water path accuracy

In Sect. 4.1, we proved that the forward operator and adjustment of the state parameters closely match with clear-sky HAMP observations. In the following, we analyze the CLWP retrieval skill based on synthetic retrieval experiments (Fig. 8). Generally, the retrieval ~~is able to reproduce the real~~ approximates the true CLWP, but with a high relative uncertainty of about 125 % for CLWP below 50 $\mathrm{g\,m^{-2}}$ and growing underestimation toward high CLWP values. The high relative uncertainty of more than 100 % for low CLWP indicates the challenge in identifying thin or low-level clouds over sea ice (Turner et al., 2007). The RMSE of the synthetic experiment for low CLWP conditions can be compared with the clear-sky retrieval (Fig. 8b). At larger distances from the sea ice edge toward the Central Arctic, the clear-sky RMSE is about 30 $\mathrm{g\,m^{-2}}$, which is comparable to the RMSE estimated from the sensitivity test for low CLWP conditions. ~~The growing bias~~

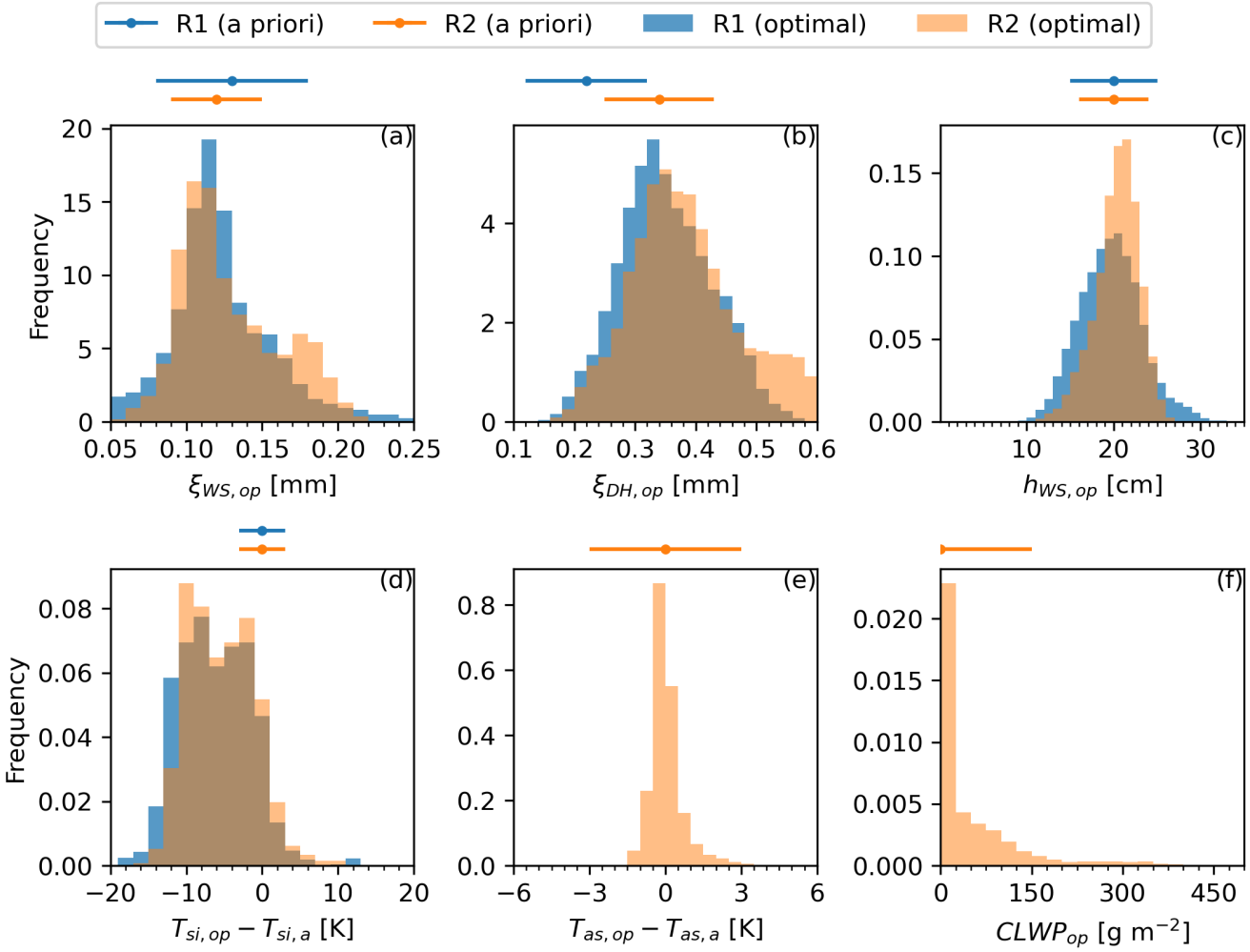

Figure 6. Histograms of the retrieved parameters from the retrievals R1 and R2 during clear-sky observations corresponding to Fig. 5. The a priori mean and uncertainty are shown above each panel. Panels show the (a) wind slab correlation length, (b) depth hoar correlation length, (c) wind slab thickness, (d) snow–ice interface temperature minus a priori, (e) air–snow interface temperature minus a priori (R2 only), and (f) cloud liquid water path (R2 only). Note that only times where both retrievals converge are shown (81 % of the data).

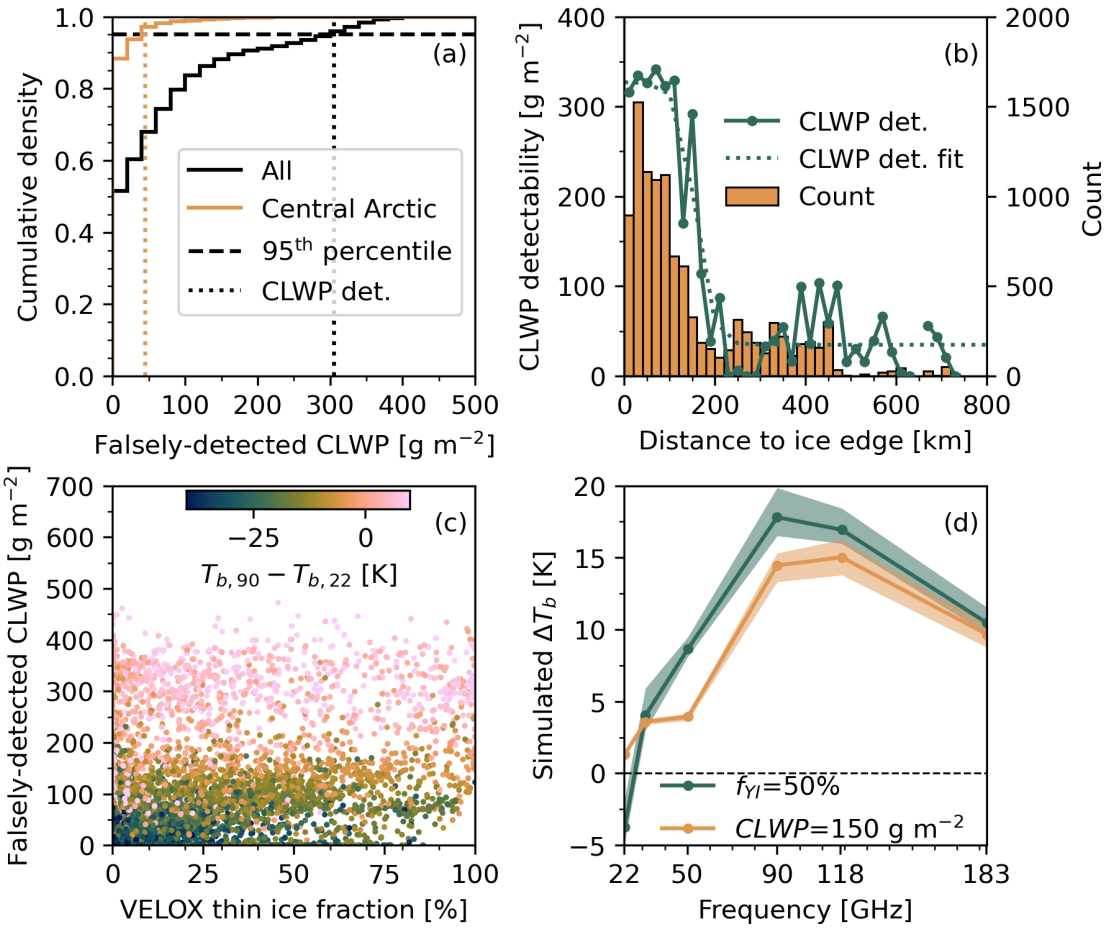

Figure 7. Assessment of cloud liquid water path (CLWP) detectability and falsely-detected CLWP. (a) Cumulative density of retrieved CLWP for all and Central Arctic clear-sky samples with the corresponding detectability estimated from the 95th percentile. (b) CLWP detectability and sigmoidal fit as a function of distance to sea ice edge. (c) Scatter plot between thin ice fraction derived from the thermal infrared spectral imager and falsely-detected CLWP with T_b difference between 90 and 22 GHz as shading. (d) Simulated brightness temperature difference (ΔT_b) between the a priori state and modified a priori states with increased f_{YI} (from 0 to 50 %) and CLWP (from 0 to 150 g m^{-2}) for all clear-sky samples. Shading indicates the 25–75 percentile range of ΔT_b for both sensitivity tests.

The growing underestimation toward high CLWP values can ~~likely~~ be explained by the ~~retrieval starting with cloud-free conditions a priori~~choice of a clear-sky a priori mean (not shown). As the ~~CLWP exceeds multiples of its uncertainty, a growing fraction of the cloud liquid signal influences the retrieval of snow parameters with similar Jacobians, particularly the~~ true CLWP exceeds the a priori mean by multiples of the a priori standard deviation, the model increasingly underestimates the true CLWP. Similar results are found for an overestimation of the true CLWP by the a priori. To understand the role of ambiguities between CLWP and other state and model parameters for the CLWP retrieval performance, we compared their residuals during synthetic experiments in Appendix D. The analysis reveals a strong correlation between CLWP and wind slab correlation length ~~(Appendix D).~~ residuals, with positive anomalies in CLWP being offset by corresponding positive anomalies in wind slab correlation length. Both residuals are correlated by 0.67, consistent with their similar spectral T_b signature (Fig. 4). Other parameters that correlate with CLWP residuals are air–snow interface temperature and wind slab density, which both influence the 90 and 118 GHz channels (Fig. 4).

The uncertainty estimated from the synthetic experiments holds for all conditions that meet the forward model assumptions. Mainly, the occurrence of leads, open water, wet snow, and deviations from the simple two-layer snow assumptions increases the CLWP uncertainty and leads to biases. However, the synthetic experiments provide the only way to assess the retrieval skill due to the lack of independent CLWP data. The good performance under clear-sky conditions provides confidence that the estimated skill closely represents real conditions. While some improvements might be expected with an improved CLWP a priori information, such as ERA5, we keep the clear-sky a priori assumption for simplicity.

We also performed sensitivity tests with two additional dual oxygen channel pairs (51.76, 52.8, 118±4.2, and 118±2.3 GHz; not shown). The lower surface sensitivity and differential water vapor emission signal were shown to provide additional information on precipitation, especially over land (Bauer and Mugnai, 2003; Bauer et al., 2005). However, the synthetic experiments did not yield an improvement in CLWP retrieval accuracy in relation to the additional computational cost. Furthermore, we increased the number of channels starting with the lower three channels (22–50 GHz) and found the highest improvement in accuracy when adding the 90 GHz channel. However, we use the entire frequency range during the retrieval to provide a broad spectral range for the surface characterization.

5 Retrieval application

5.1 Case 1: Stratocumulus (12 April 2022)

In this section, we present the HAMP retrieval for an overflight of about 800 km across a stratocumulus field over sea ice from the ice edge toward the north pole on 12 April 2022 (Fig. 9; case 1 in Fig. 1). About 92 % of the retrievals converged, which is slightly above the convergence rate of 85 % for all flights. The near and thermal infrared images indicate refrozen leads in the initial 150 km until the stratocumulus and a cirrus layer located at heights between 4–8 km (not shown) dominate the images (Fig. 9a1–b1). The cloud top height is stable with about 300–400 m along the 250 km cross section captured by *HALO* (Fig. 9b2). The radar reflectivity signal of the cloud is rather weak with few low-reflectivity streaks (Fig. 9a2).

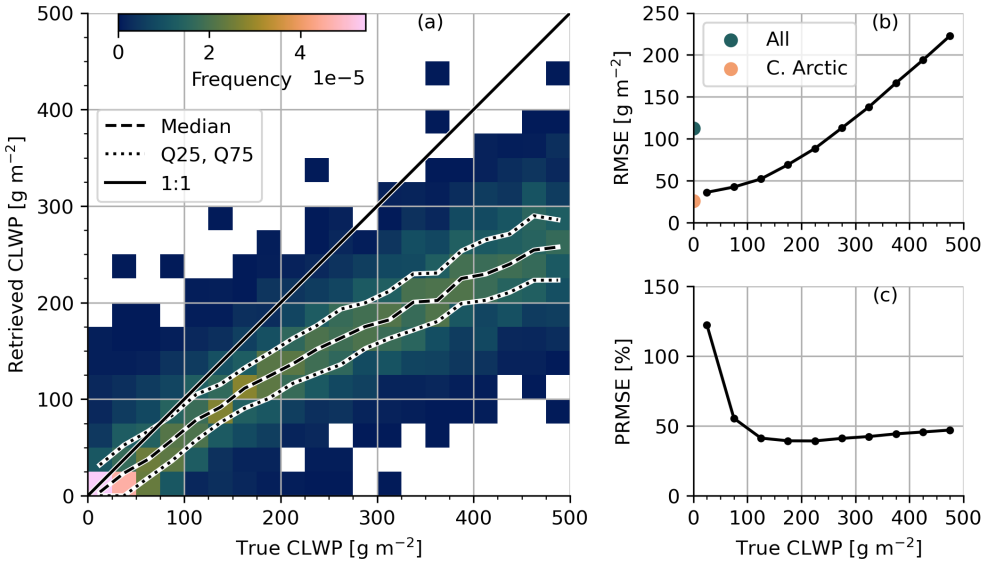

Figure 8. Cloud liquid water path (CLWP) retrieval skill based on synthetic experiments. (a) Joint histogram of the true CLWP used in the forward simulation and the retrieved CLWP, with median, 25th (Q25), and 75th percentiles (Q75). (b) Root mean squared error (RMSE) as a function of true CLWP from the synthetic experiments and clear-sky observations split into all and Central Arctic (C. Arctic) observations. (c) RMSE normalized by the true CLWP (PRMSE) as a function of true CLWP.

The observed HAMP T_b generally decreases toward the north, with a breakpoint around 400 km at 22, 31, and 50 GHz (Fig. 9c1-h1). This large-scale gradient might be related to a transition in the snow and sea ice regime toward the Central Arctic with predominantly perennial sea ice, apart from surface cooling. Small-scale features at a scale below 25 km indicate snow and sea ice variations at floe scales and the presence of refrozen leads, which likely cause the high 90, 118, and 183 GHz T_b peaks. The retrieval is able to find a matching T_b for most conditions, which represents this small and large scale T_b variability not represented by the a priori. An exception is the section from 450–600 km with differences of about 5–10 K, especially at 90, 118, and 183 GHz.

While no distinct cloud emission signature can be identified from the observed T_b time series, the retrieval finds CLWP from 0–400 km and 650–850 km. Very high and short CLWP peaks coincide with leads due to the similar Jacobians of lead fraction and CLWP (see Fig. 7d). The broader CLWP plateau from 150–400 km might be linked to actual cloud liquid presence in the stratocumulus field. However, most CLWP values are below the CLWP detectability. The CLWP signal at the end of the segment does not align with an observed liquid layer in the lidar. The other state parameters follow the small and large scale T_b features discussed earlier. Notably, the depth hoar correlation length increases around 400 km, which could be linked to more multiyear ice toward the north. Interestingly, the wind slab correlation length does not follow the same pattern and increases around 600 km.

Overall, this case study demonstrates that the retrieval finds a state space, which matches the observations under cloudy and clear-sky conditions along a long flight segment from the sea ice edge to the Central Arctic (81–88° N). However, the retrieval does not clearly identify the CLWP signature of the low-level stratocumulus field, likely due to its CLWP being below the CLWP detectability threshold, and falsely retrieves CLWP in areas without liquid cloud layers.

5.2 Case 2: Warm air intrusion (14 March 2022)

After analyzing the HAMP retrieval for a stratocumulus cloud with low CLWP, we now present a second case during a crossing from north to south of the warm air intrusion on 14 March 2022 (Fig. 10; case 2 in Fig. 1). Almost all of the retrievals converged along this transect (99 %). The radar shows the cloud and precipitation structure with snowfall occurring from 25–175 km. The lidar signal shows liquid top heights from 2–4 km within the precipitating system. Lower clouds occur toward the end of the segment. These clouds can also be seen in the near-infrared images. The thermal infrared images indicate increased fraction and size of leads with warmer skin temperature than the surrounding sea ice toward the end of the segment, around 550 km.

The observed HAMP T_b decreases toward the end of the segment at all frequencies, which is partly linked to the decrease in atmospheric water vapor and temperature as *HALO* leaves the warm air intrusion center. This gradient is also reflected by the a priori T_b. However, the T_b decreases well below the a priori at all frequencies with sharp boundaries at about 200 and 425 km. Similar to the stratocumulus case in Fig. 9, the observations and the simulated optimal state align well on both small and large spatial scales. Larger differences between the observations and retrieved state occur between 250–450 km. Moreover, the simulation overestimates the observed 22 GHz T_b from 200 km until the end of the segment.

The retrieval adds CLWP for regions where the lidar also identifies liquid layers with up to 300 $\mathrm{g\,m^{-2}}$ from 0–225 km. This region corresponds to the cloudy region at the core of the warm air intrusion and is partly excluded from the retrieval due to potential scattering by frozen hydrometeors that are not considered in the radiative transfer. The decrease in CLWP also aligns with the transition from liquid to non-liquid layers in the lidar backscatter ratio. Also, ERA5 data contains clouds with CLWP up to about 75 $\mathrm{g\,m^{-2}}$, although a comparison is challenging due to the larger size of the model grid compared to the HAMP footprint. The retrieved CLWP toward the end of the segment is likely associated with the low-level clouds and false detections from refrozen leads, which formed in response to the warm air intrusion.

The air–snow interface temperature aligns generally well with the KT-19 skin temperature with absolute differences mostly below 2 K. ~~The~~ However, both temperatures diverge from about 425–525 km with the KT-19 being warmer and the retrieved value colder than the a priori. The reduction of the retrieved air–snow interface temperature at 425 km aligns with a reduction of the T_b at 50–183 GHz. Similarly, the snow–ice interface temperature drops to very low values at about 200 km, corresponding to the 22 GHz T_b decrease. A similar trend can be found for the wind slab and depth hoar correlation lengths, which increase toward the end of the segment at about 425 km. The wind slab correlation length is very low within the precipitating system, likely due to the ambiguity with the CLWP signal (see Appendix D). Overall, the ~~liquid cloud signal~~ occurrence of liquid clouds during the warm air intrusion is well ~~represented~~ captured by the retrieval.

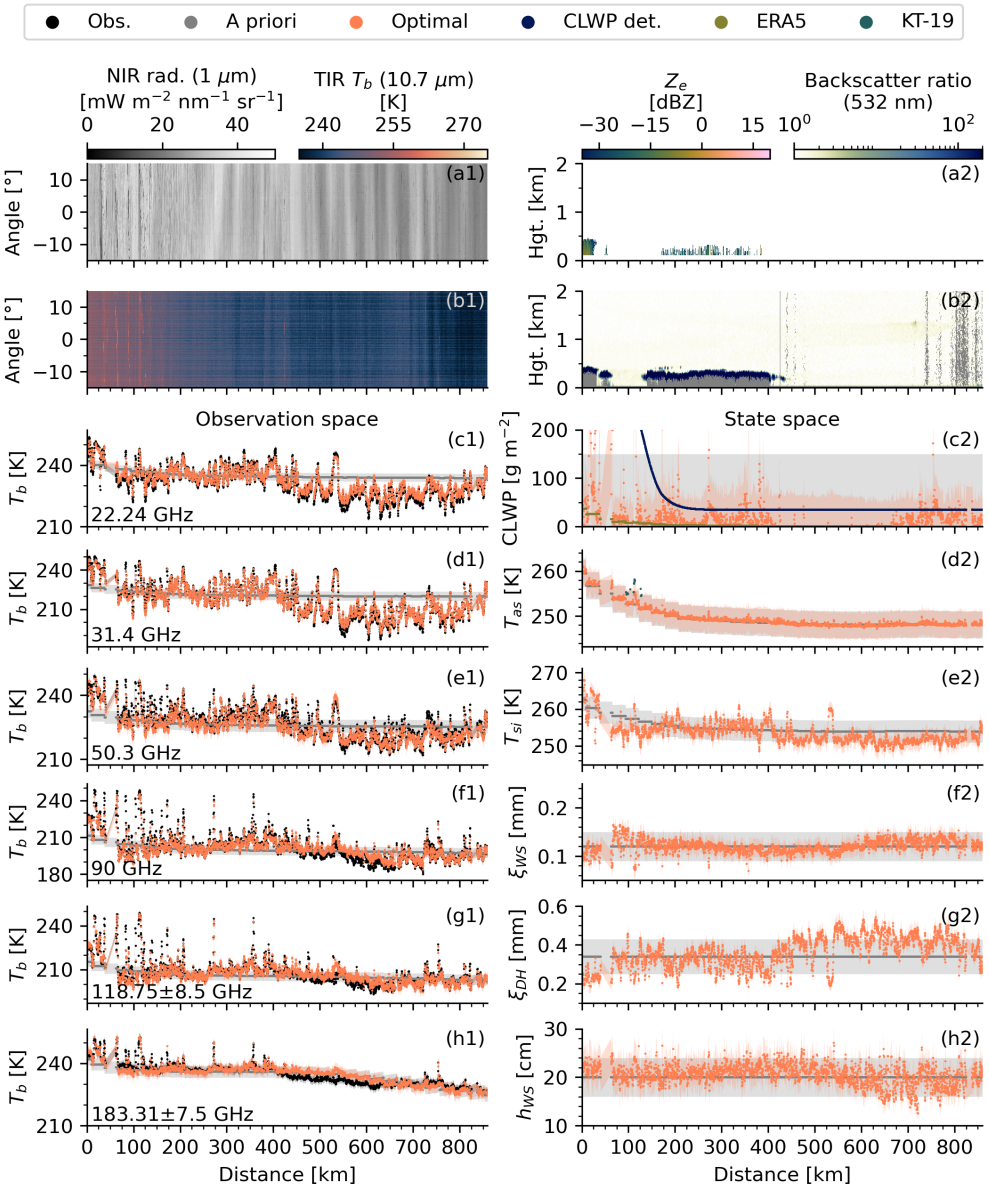

Figure 9. HAMP observation and retrieval for a northbound flight segment above a stratocumulus field on 12 April 2022 (case 1 in Fig. 1). (a1) Near infrared radiance, (a2) radar reflectivity, (b1) thermal infrared T_b, and (b2) backscatter ratio. (c1-h1) Observation space: Observed, a priori, and optimal T_b at (c1) 22, (d1) 31, (e1) 50, (f1) 90, (g1) 118, and (h1) 183 GHz. (c2-h2) State space: A priori and optimal (c2) cloud liquid water path from HAMP with ERA5 cloud liquid water path and HAMP cloud liquid water path detectability (CLWP det.), (d2) air–snow interface temperature with KT-19 skin temperature under clear-sky, (e2) snow–ice interface temperature, (f2) wind slab correlation length, (g2) depth hoar correlation length, and (h2) wind slab thickness. The shading in panels c–h indicates the measurement uncertainty (observation), effective measurement uncertainty (radiative transfer simulations), a priori uncertainty (a priori state), and retrieval uncertainty (optimal state). Note that the CLWP detectability exceeds the axis limit from 0–100 km.

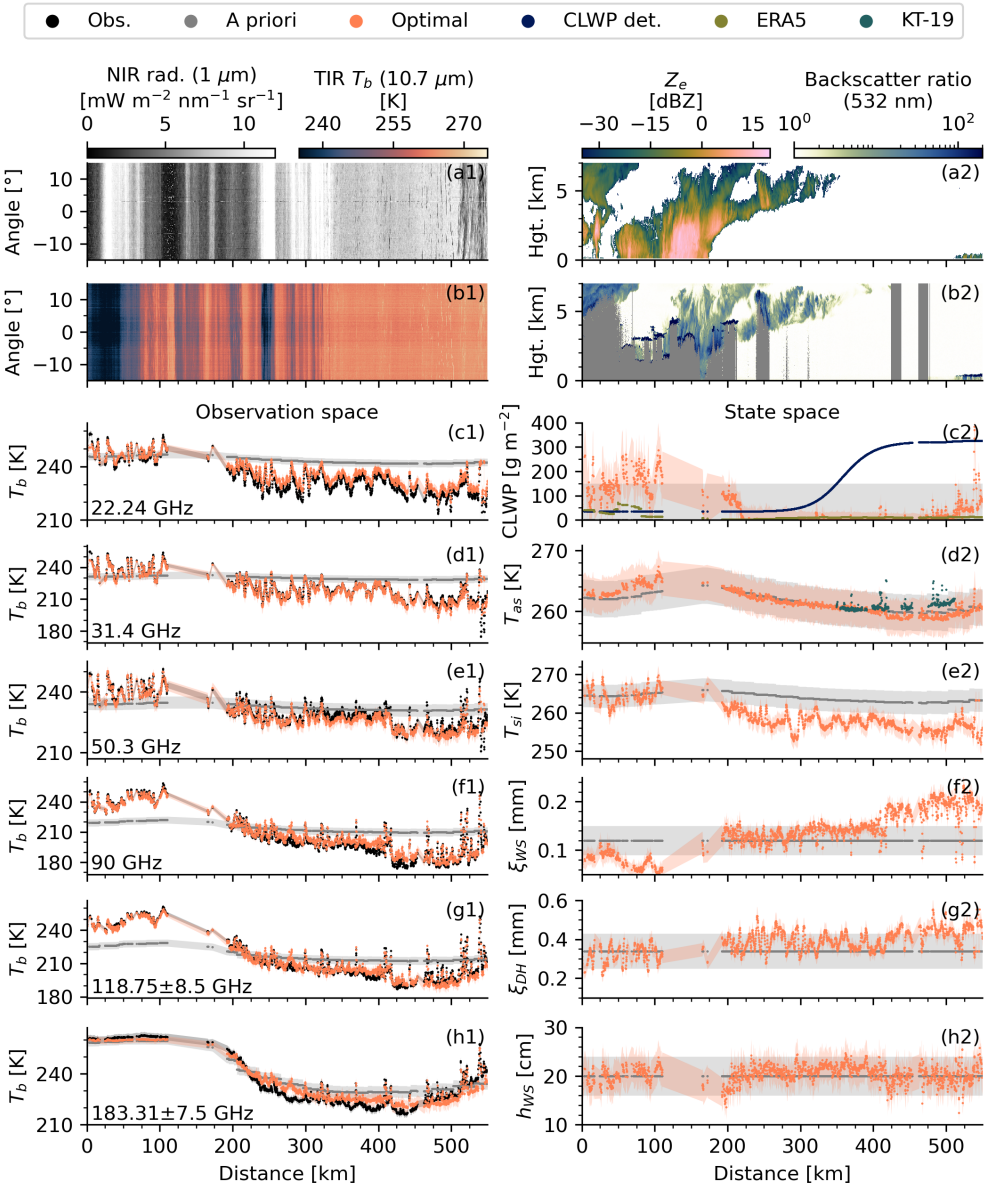

Figure 10. HAMP observation and retrieval for a southbound flight segment during the warm air intrusion on 14 March 2022 (case 2 in Fig. 1). Panels as in Fig. 9.

5.3 Rain-on-snow event (12–14 March 2022)

Sea ice parameters retrieved during the warm air intrusion on 14 March 2022 partly lie outside of the expected parameter range. This flight covered an area affected by surface melt and rain on 13 March 2022 and subsequent refreezing. It is well known that rain-on-snow (ROS) events and associated surface glazing strongly influence the sea ice microwave signature from ground-based (Stroeve et al., 2022) and satellite observations (Voss et al., 2003; Rückert et al., 2023a). In the following, we present the evolution of the state parameters during three consecutive flights from 12 to 14 March 2022, covering the conditions before, during, and after the ROS event (Fig. 11). The 91 GHz V-pol imagery captured by SSMIS onboard DMSP-F16 close to the *HALO* overpasses shows an increase in T_b by several tens of Kelvins from 12 to 13 March 2022. After the ROS event on 14 March 2022, the T_b decreases far below the condition observed prior to the ROS event (Fig. 11a3), and remains low for a couple of weeks until April 2022 (not shown).

The HAMP retrieval on 12 March lies near the a priori values and converges 87 % of the time. The only outlier is an open water patch near the ice edge at 80° N, which corresponds to very low T_b that causes artificial sharp gradients in the retrieved snow–ice interface temperature and depth hoar correlation length. The cloudy region south of 82° N visible in radar and lidar is captured by the retrieval. The retrieved CLWP reaches mostly values between 200 and 300 $\mathrm{g m^{-2}}$, which aligns with liquid layer top heights of 4–5 km detected by the lidar.

On 13 March, a clearly visible bright band at 1 km height in the radar reflectivity profile likely indicates melting snow and associated rainfall on the sea ice. Therefore, the retrieval is invalid for most parts of this segment and masked out by the 2 m air temperature and radar reflectivity flags. The northern part of the bright band is not flagged at about 83° N, but the HAMP retrieval does not converge in this area (Fig. 11a2). The area not affected by the ROS event (north of 83° N) mostly lies close to the a priori. A notable increase in the depth hoar correlation length north of 86° N might be related to the higher fraction of perennial sea ice.

After the ROS event, the HAMP retrieval converged for most observations (99 %) on 14 March (see Sect. 5.2). While sea ice parameters in the northern region lie close to the a priori, they deviate from the expected range in the low-T_b region south of 84.5° N (Fig. 11a3). This is slightly farther north than the observed melting layer in the radar at 83° N and could be explained by the northward transport of warm and moist air masses between the flights and potential rain or surface melt up to 84.5° N. Especially the wind slab correlation length and the snow–ice interface temperature lie far from the a priori and the conditions observed before the ROS event on 12 March. Potential reasons for the altered sea ice emissivity could be the formation of ice lenses after the freeze-up at the surface. Ice lenses are weakly scattering and lower the microwave emissivity through the dielectric contrasts between adjacent layers of different densities. Additionally, newly accumulated snow on top of the ice lens could amplify the T_b reduction. Interestingly, a secondary increase in the wind slab correlation length ~~occurs~~ and a small reduction in the air–snow interface temperature occur as *HALO* approaches the T_b minimum of the SSMIS swath around 82.5° N. Near and thermal infrared images do not show apparent surface patterns that correlate with this microwave signature (not shown). Thus, we assume that spatial variations of snowpack changes (ice lens, fresh snow) contribute.

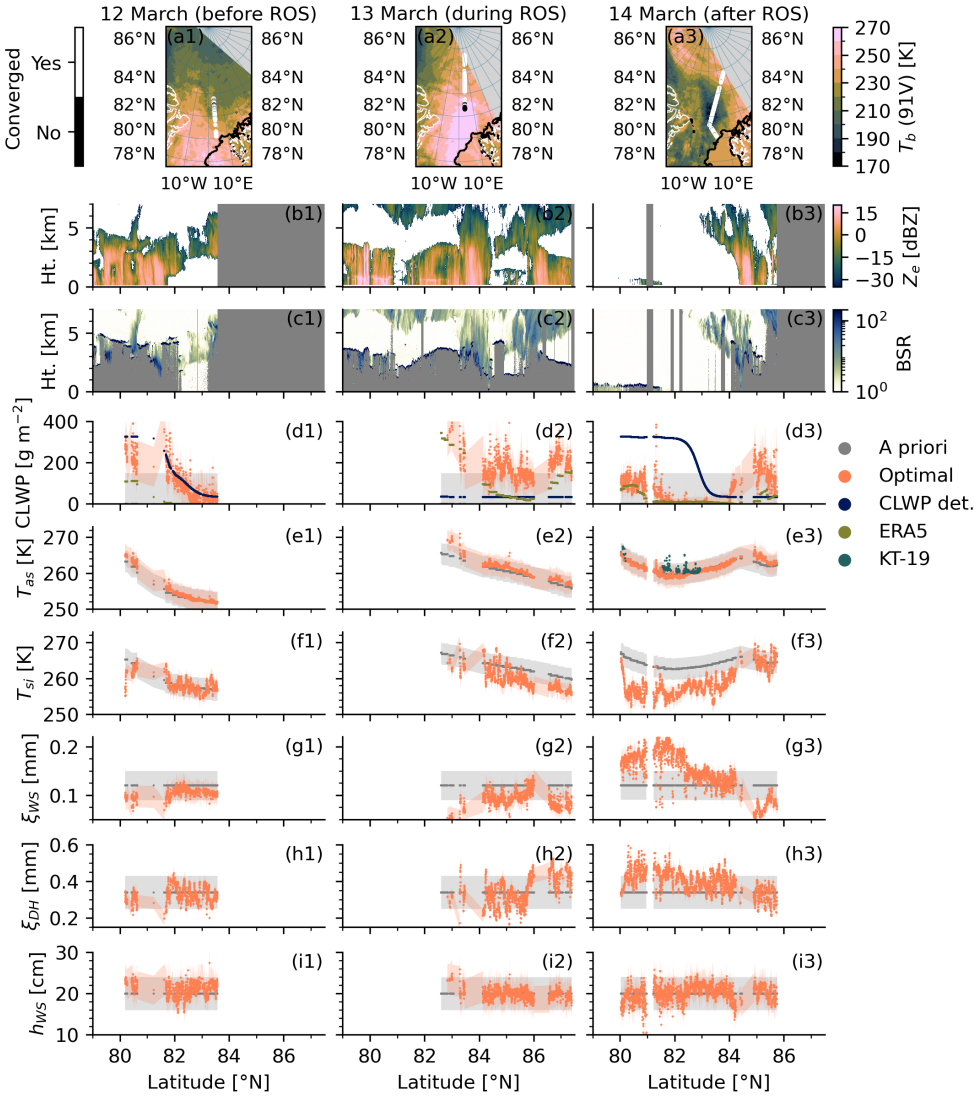

Figure 11. HAMP retrieval and satellite observations before the rain-on-snow (ROS) event (12 March 2022, column 1), during the ROS event (13 March 2022, column 2), and after the ROS event (14 March 2022, column 3). (a1–a3) 91 GHz V-pol T_b from SSMIS onboard DMSP-F16 at about (a1) 13:30 UTC, (a2) 15:00 UTC, and (a3) 14:45 UTC, 15 % sea ice concentration contour, and meridional *HALO* flight tracks with retrieval convergence mask as shading from (a1) 13:56–15:42 UTC, (a2) 13:43–15:30 UTC, and (a3) 13:26–16:45 UTC. Note that *HALO* flew a zonal segment during the turn in (a3), not shown here. Panels below the maps show *HALO* observations and retrieval parameters (a priori and optimal) as a function of latitude: (b1–b3) Radar reflectivity, (c1–c3) backscatter ratio (BSR), (d1–d3) cloud liquid water path from HAMP with ERA5 cloud liquid water path and HAMP cloud liquid water path detectability (CLWP det.), (e1–e3) air–snow interface temperature with KT-19 skin temperature under clear-sky, (f1–f3) snow–ice interface temperature, (g1–g3) wind slab correlation length, (h1–h3) depth hoar correlation length, and (i1–i3) wind slab thickness. The shading in panels d–i indicates the a priori uncertainty (a priori state) and retrieval uncertainty (optimal state).

5.4 CLWP variability during HALO–$(\mathcal{AC})^3$

In this section, we exploit the collocated radar–lidar cloud remote sensing data from *HALO* to assess CLWP distributions for different cloud types (Fig. 12). In total, 85 % of HAMP retrievals converge during the entire campaign, which is similar to the clear-sky convergence rate (87 %). For better comparability between HAMP and ERA5, we resample hourly-mean CLWP from HAMP and CLWP from the nearest ERA5 grid cell to a $31 \times 31\,\mathrm{km}^2$ Equal-Area Scalable Earth (EASE) Grid 2.0 (Brodzik et al., 2012). The CLWP distributions of HAMP shift gradually toward higher values with increasing liquid top height determined from the lidar (Fig. 12a). The low liquid top class predominantly shows CLWP below $25\,\mathrm{g\,m^{-2}}$ and the high liquid top class shows a broad peak from ~~100–200~~100–250 $\mathrm{g\,m^{-2}}$. During the absence of a liquid layer, the CLWP follows the clear-sky distributions (Fig. 6f) with a considerable amount of falsely detected CLWP likely related to refrozen leads. To exclude these cases, we filter for the Central Arctic, where fewer leads are expected (Fig. 12c). The ~~no liquid class~~ no-liquid-class remains mostly below $50\,\mathrm{g\,m^{-2}}$, which aligns with the lower CLWP detectability threshold found in this region. Most CLWP values above $100\,\mathrm{g\,m^{-2}}$ align with observations with liquid top heights between 1–5 km. ~~In the 50–100 range, the 0.5–1 liquid top heights become more frequent.~~

The distributions from ERA5 follow a similar shape as the HAMP distributions for all observations (Fig. 12b) and the Central Arctic (Fig. 12d). A notable difference for all cases is the higher number of extremes derived from HAMP, which likely relates to the ~~small footprint size of HAMP with 1 compared to a spatial resolution of~~ limited coverage of the 31×31 ~~of ERA5~~km^2 grid cell by HAMP's narrow beam. Moreover, potential false detection over leads could cause artificial CLWP peaks. ~~Both CLWP distributions peak at 125–150~~ However, both datasets show a similar range of CLWP values when a liquid layer was detected by the lidar between 1–5 km. For the distribution in the Central Arctic, both HAMP and ERA5 show CLWP up to ~~175~~200 $\mathrm{g\,m^{-2}}$ and a few extremes above ~~200~~250 $\mathrm{g\,m^{-2}}$ mostly linked to high liquid tops. The higher correlation between HAMP and ERA5 in the Central Arctic (0.79) compared to all observations (0.51) likely reflects the improved accuracy of HAMP in this region.

The analysis of CLWP distributions for HAMP and ERA5 indicates agreement in both the shape and magnitude of CLWP. However, the relatively high uncertainty of the HAMP retrieval and the negative bias found for high CLWP from synthetic experiments should be considered when evaluating ERA5 CLWP.

6 Conclusions

Passive microwave observations provide high spatial and temporal coverage in the Arctic onboard polar orbiting satellites, but their use remains limited due to the variable sea ice and snow emission. Here, we exploited nadir-viewing passive microwave observations (22–183 GHz) and collocated active cloud remote sensing data for diverse cloud and sea ice conditions captured with the *HALO* aircraft during the Arctic spring HALO–$(\mathcal{AC})^3$ campaign (Wendisch et al., 2024). We developed a physical sea ice–atmosphere optimal estimation retrieval algorithm with the loosely coupled SMRT (Picard et al., 2018) and PAMTRA (Mech et al., 2020) radiative transfer models for the HAMP microwave radiometer channels. The algorithm retrieves three snow layer parameters (wind slab correlation length, depth hoar correlation length, and wind slab thickness), the air–snow and snow–ice interface temperatures, and CLWP. The combination of this passive microwave retrieval with *HALO's* cloud

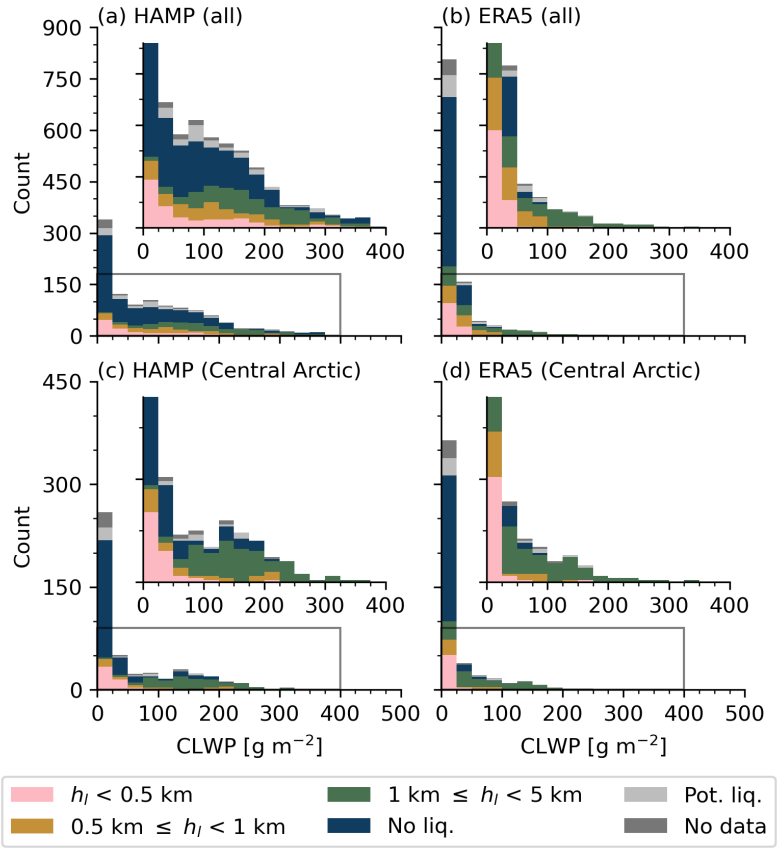

Figure 12. ~~Cloud~~ Hourly mean cloud liquid water path histogram along the HALO flight track from (a, c) HAMP and (b, d) ERA5 resampled to a 31×31 km^2 equal-area grid. (a, b) All observations and (c, d) observations in the Central Arctic. Shading classifies observations based on liquid top height (h_l), no liquid (No liq.), potential liquid (Pot. liq.), and missing lidar data. The inset region is denoted by the gray rectangle. Note that ERA5 is only shown for times where the HAMP retrieval converged.

observatory instrument suite, which is typically not available for passive microwave observations from satellites, provides a unique opportunity to (1) assess the representation of sea ice and snow microwave emission by the forward model, (2) estimate the CLWP detectability and retrieval accuracy, and (3) analyze the spatial variability of CLWP over sea ice during HALO–$(\mathcal{AC})^3$.

The optimal estimation retrieval found a geophysical state consistent with HAMP clear-sky observations identified by the collocated radar–lidar cloud mask with a convergence rate of 87 %. The T_b departure of the optimal solution strongly improved compared to the a priori, which assumed no spatial variability of the three snow properties. Moreover, the distributions of all snow parameters lie within the expected range.

The CLWP detectability was assessed from the clear-sky performance. We find a detectability threshold of 50 g m^{-2} in the Central Arctic, which increases towards the marginal ice zone up to 350 g m^{-2}. The detectability near the marginal ice zone

can be potentially improved with additional information on lead or young ice fraction. From SMRT–PAMTRA simulations, we found that a young ice fraction of 50 % causes a similar T_b signature as 150 g m^{-2} CLWP. The CLWP retrieval accuracy was derived from synthetic retrieval experiments. The relative root mean squared error of CLWP decreased from above 100 % for CLWP below 50 g m^{-2} to below 50 % above 100 g m^{-2}. The identified bias for higher CLWP values can be explained by the parameter ambiguity between CLWP and wind slab correlation length, as well as the clear-sky a priori assumption.

The retrieval was applied to a stratocumulus case and a warm air intrusion case. While the CLWP of the stratocumulus case was mostly near the detectability threshold and not clearly matching with the liquid layer visible in the lidar observations, the higher CLWP of the warm air intrusion event aligned well with the lidar. The simultaneously derived surface parameters for the stratocumulus case follow realistic spatial gradients with increased snow correlation length and thus increased scattering from the ice edge toward the north pole. A statistical comparison of CLWP for all flights between HAMP and ERA5 ~~found generally a similar CLWP shape~~ revealed a correlation of 0.79 in the Central Arctic (0.51 for all observations), a similar CLWP distribution shape, and increasing CLWP for increasing liquid top height.

~~This work implies that SMRT could be useful in a~~ The results of this work demonstrate that inversion of the coupled sea ice–atmosphere ~~data assimilation system using a priori data from a thermodynamic sea iceand snow evolution model. This approach would benefit from the high sensitivity of passive microwave observations to snow emissivity changes due to atmospheric processes, such as rain, snowfall, and near-surface air temperature. For example, the warm air intrusion in March 2022 and the associated surface melt and rain-on-snow event altered the emissivity within a few hours due to increased liquid water fraction within the snowpack, and the subsequent refreezing and potential ice lens formation altered the T_b signature for several weeks compared to conditions prior the warm air intrusion~~observation operator SMRT–PAMTRA allows for the retrieval of CLWP over Arctic sea ice. The highest retrieval skill is found for high-CLWP conditions during warm air intrusions. Under conditions with stratiform clouds with lower CLWP, which frequently occur during Arctic winter (e.g., Walbröl et al., 2022), the CLWP retrieval is more uncertain. The representation of the surface properties using static sea ice and snow a priori assumptions, as done in this work, serves as a baseline for coupling SMRT–PAMTRA with output from thermodynamic sea ice and snow evolution models.

There are several limitations of this study, apart from the limited seasonal and spatial generalization of field observations. First, no independent quantitative reference observations of the state variables exist at scale, especially under cloudy conditions and regarding snow microstructure. The second limitation involves the simplified two-layer snowpack without fresh surface snow from accumulating snow or ice lenses from melt-freeze cycles, which both impact the emissivity at frequencies sensitive to CLWP (e.g., Sandells et al., 2024). The difficulty of simulating these scattering signatures with our two-layer snow setup might partly explain the non-convergence rate of 13 % under clear-sky conditions.

~~A way for future work to advance the use of passive microwave observations in the Arctic lies in exploiting the influence of atmospheric events on surface emission, such as rain-on-snow, and the integration of~~ Future work could integrate more observation geometries from microwave imagers and sounders ~~. This would not only increase the temporal resolution , which is crucial during extreme events like warm air intrusions, but also ensure~~ to enhance temporal resolution and spectral, angular, and polarization consistency of the radiative transfer simulations. Especially the angular and polarization dependence over

sea ice could provide additional information benefit for integrated sea ice–atmosphere retrievals, but requires validation of SMRT, e.g., using ship observations (Rabe and Geibert, 2025; Rückert et al., 2025)~~, and could provide additional information benefit for integrated sea ice–atmosphere retrievals~~. Finally, replacing the static sea ice and snow a priori with thermodynamic model output could improve CLWP retrieval accuracy by representing spatial and temporal variability in the sea ice and snow properties.

Code and data availability. The code for this study is available on Zenodo at https://doi.org/10.5281/zenodo.18237101 (Risse, 2026). The optimal estimation retrieval inputs and outputs are available on Zenodo at https://doi.org/10.5281/zenodo.15848709 (Risse, 2025). The version of PAMTRA with an emissivity vector extension corresponds to commit fb71f43 (last access: 21 November 2024), pulled from https://github.com/nrisse/pamtra/commit/fb71f43 (Mech et al., 2020). The version of SMRT corresponds to commit 6f7dadc (last access: 29 October 2024), pulled from https://github.com/smrt-model/smrt/commit/6f7dadc (Picard et al., 2018). The version of pyOptimalEstimation corresponds to commit 1eb4f26 (last access: 22 November 2024), pulled from https://github.com/maahn/pyOptimalEstimation/commit/1eb4f26 (Maahn et al., 2020). HAMP measurements were obtained from https://doi.org/10.1594/PANGAEA.974108 (Dorff et al., 2024). WALES measurements were obtained from https://doi.org/10.1594/PANGAEA.967086 (Wirth and Groß, 2024). KT-19 measurements were obtained from https://doi.org/10.1594/PANGAEA.967378 (Schäfer et al., 2024). VELOX measurements were obtained from https://doi.org/10.1594/PANGAEA.963382 (Schäfer et al., 2023b). SpecMACS measurements were obtained from https://doi.org/10.1594/PANGAEA.966992 (Weber et al., 2024b). Dropsonde measurements were obtained from https://doi.pangaea.de/10.1594/PANGAEA.968900 (George et al., 2024). The VELOX surface classification data were obtained from https://doi.org/10.1594/PANGAEA.974454 (Müller et al., 2025a). Aircraft position and orientation were obtained from the "ac3airborne" intake catalog (Mech et al., 2022). The sea ice concentration data from the University of Bremen were obtained from https://data.seaice.uni-bremen.de (last access: 30 April 2025, Spreen et al., 2008). The ERA5 reanalysis data on model levels were obtained from https://doi.org/10.24381/cds.143582cf (last access: 28 June 2025, Hersbach et al., 2017). The ERA5 reanalysis data on single levels were obtained from https://doi.org/10.24381/cds.adbb2d47 (last access: 28 June 2025, Hersbach et al., 2023). The Level 1C T_b data for SSMIS on DMSP-F16 were obtained from https://doi.org/10.5067/GPM/SSMIS/F16/1C/07 (Berg, 2021).

Appendix A: Atmospheric profiles

The approach of fixed atmospheric temperature and specific humidity profiles differs from sea ice–atmosphere retrievals that derive temperature profiles (Kang et al., 2023) or integrated water vapor (IWV) (Rückert et al., 2023b) based on climatological mean a priori data. The collocated instantaneous ERA5 data provide accurate IWV when compared to dropsondes launched over sea ice with a root mean squared error (RMSE) of 0.25 $\mathrm{kg\,m^{-2}}$ and percentage RMSE (PRMSE) of 9 $\%$, without notable improvement for assimilated dropsondes. Similarly low RMSE between ERA5 and dropsondes over sea ice are found for profiles of temperature (0.5 K above 1 km height and up to 2 K below 1 km height) and relative humidity (10–15 $\%$) (see Fig. 3 in Walbröl et al., 2024). To assess the impact of ERA5 IWV uncertainty at HAMP frequencies, we conduct a sensitivity test by increasing IWV by 10 $\%$. This test results in maximum T_b changes of up to 2 K at 183$\pm$7.5 GHz for IWV ranges of 2 to

$4\,\mathrm{kg\,m^{-2}}$ and 1.5 K at 118±8.5 GHz for IWV ranges of 8 to $13\,\mathrm{kg\,m^{-2}}$ (not shown). These relatively moderate sensitivities support our use of fixed atmospheric profiles.

Appendix B: A priori interface temperatures

The snow–ice interface temperature (T_{si}) a priori is computed by a simple linear scaling between the air–snow interface temperature a priori (T_{as}) and the water temperature ($T_w = 271.35K$) with a manually determined scaling factor ($a = 0.25$), chosen from sensitivity tests, as

$$T_{si} = T_{as} + a \cdot (T_w - T_{as}). \tag{B1}$$

The ERA5-based air–snow interface temperature a priori used in R2 is derived from ERA5 skin temperature ($T_{s,ERA5}$) with an empirical correction to remove biases with respect to the KT-19 skin temperature. We derive the following empirical relationship from clear-sky HALO–$(\mathcal{AC})^3$ data:

$$T_{as} = 0.94 \cdot T_{s,ERA5} + 11\,\mathrm{K}. \tag{B2}$$

Appendix C: Inter-channel T_b correlations from observations and R1

Differences between the observed and simulated inter-channel T_b correlations provide insights into the accuracy of spectra simulated using the SMRT–PAMTRA forward operator. Here, we compare simulations of the optimal state of the clear-sky R1 retrieval with corresponding HAMP observations for all cases and for Central Arctic cases (Fig. C1). The observed correlation is highest for adjacent window channels, while it is lowest between the 22 and 183 GHz channels. A similar pattern is also present in the SMRT–PAMTRA simulations. Especially the frequency range from 31–118 GHz, which includes two channels with the highest sensitivity to CLWP (see Fig. 4), the simulations represent the observed inter-channel correlations within ±0.1. However, simulated inter-channel correlations involving the 22 GHz channel (for all cases) and the 183 GHz channel (for Central Arctic cases) are higher than those observed. The highest difference occurs between 22 and 183 GHz with 0.15 (0.2) in the observations and 0.57 (0.52) in the simulations for all (Central Arctic) cases. Hence, there appears to be a limitation in the retrieval that prevents the independent adjustment of both channels. As these channels correspond to the lowest and highest penetration depths (Tonboe et al., 2006), the difference may be explained by a lack of state parameters that modify the uppermost and lowermost parts of the snowpack or the sea ice. However, the impact of this missing independence between the 22 and 183 GHz channels is expected to have a negligible impact on the CLWP retrieval.

Appendix D: Parameter ambiguities

In the following, we analyze parameter ambiguities between the six retrieved state parameters and the four fixed model parameters from synthetic retrievals. The ambiguities are quantified from correlations between the normalized residuals derived for

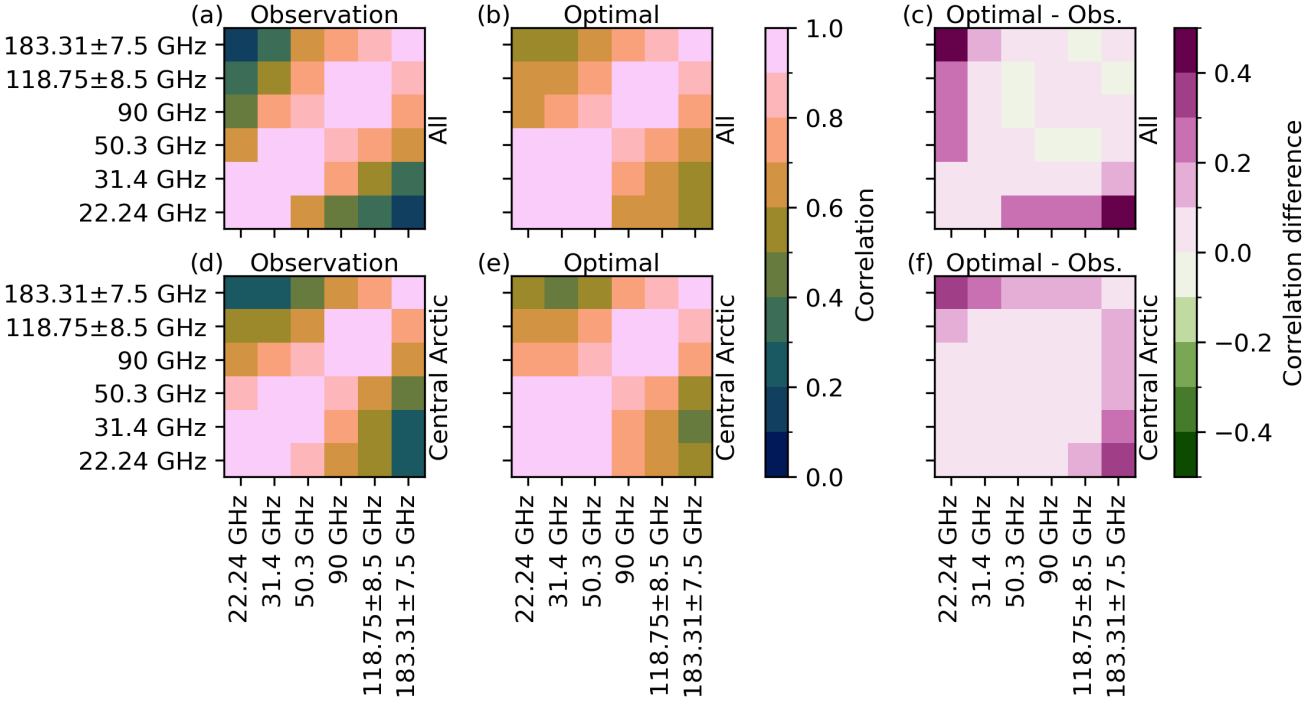

Figure C1. Inter-channel T_b correlations from (a, d) HAMP observations, (b, e) optimal state simulations from R1, and (c, f) differences between the correlation from observed and optimal state simulations from R1 for (a–c) all and (d–f) Central Arctic observations.

the state parameters as

$$r_{x,i} = \frac{x_{op,i} - x_{true,i}}{\sqrt{S_{a,ii}}}, \tag{D1}$$

with the retrieved state x_{op} and state used for the synthetic observation x_{true}. The same equation is adapted to the model parameters, which are fixed during the retrieval, i.e,

$$r_{b,i} = \frac{b_i - b_{true,i}}{\sqrt{S_{b,ii}}}, \tag{D2}$$

where b_{true} denotes the model parameter used for the synthetic observation. Correlations between two model parameters are neglected here as they are not directly relevant for the retrieval performance.

In total, 14 out of 39 parameter combinations show correlations larger than ± 0.1, and five of the relationships include CLWP (Fig. D1). The highest correlation is found between CLWP and wind slab correlation length (0.67). This indicates that scattering in the wind slab layer partly compensates the spectral cloud emission signature and vice versa. This is consistent with similar Jacobians, which indicates that both parameters affect the simulated T_b in a similar way (not shown). Also, the posterior covariance matrix shows a high correlation of 0.8 between CLWP and wind slab correlation length. Negative correlations are found between CLWP and air–snow interface temperature (-0.21) and wind slab density (-0.18). Minor relationships occur

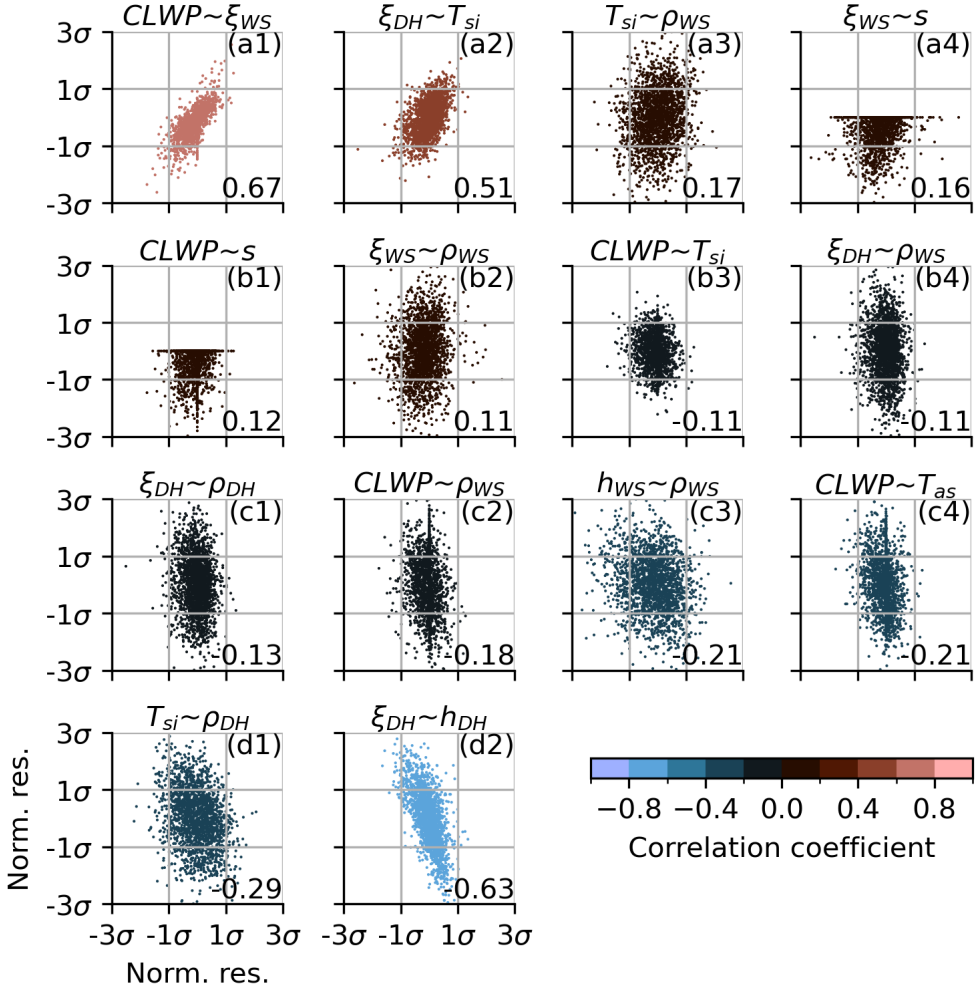

Figure D1. Correlations between normalized parameter residuals from the synthetic retrieval experiment. The parameter combinations are sorted from positive to negative correlations, and the first (second) parameter is shown on the horizontal (vertical) axis. Note that parameter combinations with correlations within ±0.1 are not shown and that no positive residuals occur for the specularity model parameter. Parameter names of each symbol are listed in Table 2.

between CLWP and the specularity parameter and snow–ice interface temperature. The lower correlation with these parameters can be related to the larger differences in the Jacobian matrix. Correlations between other parameters are also found, notably between depth hoar correlation length and depth hoar thickness (-0.63) and snow–ice interface temperature (0.51). Overall, the pronounced ambiguity between CLWP and wind slab correlation length suggests that HAMP observations can only partly separate both signals over sea ice from real observations.

Author contributions. NR conducted the retrieval, data analysis, and visualization, and prepared the manuscript. SC, MM, CP, and NR conceptualized the study. SC, MM, and NR carried out the field observations. JM derived the VELOX surface classification within the radiometer footprint. All authors reviewed and edited the manuscript.

Competing interests. The authors declare that they have no conflict of interest.

Acknowledgements. We gratefully acknowledge the funding by the German Research Foundation [Deutsche Forschungsgemeinschaft (DFG)] of the Transregional Collaborative Research Center SFB/TRR 172 "Arctic Amplification: Climate Relevant Atmospheric and Surface Processes, and Feedback Mechanisms $(\mathcal{AC})^3$" (Project-ID 268020496). The authors are grateful to the AWI for providing and operating the two Polar 5 and Polar 6 aircraft. We thank the crews and the technicians of the three research aircraft for excellent technical and logistical support. The generous funding of the flight hours for the Polar 5 and Polar 6 aircraft by AWI and for HALO by the DFG, Max-Planck-Institut für Meteorologie (MPI-M), and Deutsches Zentrum für Luft- und Raumfahrt (DLR) is greatly appreciated. We are further thankful for the funding provided by DFG within the framework of Priority Program (SPP 1294) to promote research with HALO (grant no. 316646266). We would like to thank Ghislain Picard for his support on the SMRT simulation setup. Furthermore, we acknowledge the freely available Python packages, including but not limited to numpy (Harris et al., 2020), pandas (McKinney, 2010), xarray (Hoyer and Hamman, 2017), and scipy (Virtanen et al., 2020) for data analysis, and matplotlib (Hunter, 2007), seaborn (Waskom, 2021), and cartopy (UK Met Office, 2023) for visualization. We sincerely appreciate Fabio Crameri for providing scientific colormaps via an open repository, enhancing the visual quality of this work (Crameri, 2018). We acknowledge the use of large language models by OpenAI via GitHub Copilot for code generation assistance during the development of the retrieval and analysis.

References

Bauer, P. and Mugnai, A.: Precipitation profile retrievals using temperature-sounding microwave observations, Journal of Geophysical Research: Atmospheres, 108, 2003JD003 572, https://doi.org/10.1029/2003JD003572, 2003.

Bauer, P., Moreau, E., and Di Michele, S.: Hydrometeor Retrieval Accuracy Using Microwave Window and Sounding Channel Observations, Journal of Applied Meteorology, 44, 1016–1032, https://doi.org/10.1175/JAM2257.1, 2005.

Bennartz, R. and Bauer, P.: Sensitivity of microwave radiances at 85–183 GHz to precipitating ice particles, Radio Science, 38, 2002RS002 626, https://doi.org/10.1029/2002RS002626, 2003.

Berg, W.: GPM SSMIS on F16 Common Calibrated Brightness Temperatures L1C 1.5 hours 12 km V07, https://doi.org/10.5067/GPM/SSMIS/F16/1C/07, 2021.

Boukabara, S.-A., Garrett, K., Chen, W., Iturbide-Sanchez, F., Grassotti, C., Kongoli, C., Chen, R., Liu, Q., Yan, B., Weng, F., Ferraro, R., Kleespies, T. J., and Meng, H.: MiRS: An All-Weather 1DVAR Satellite Data Assimilation and Retrieval System, IEEE Transactions on Geoscience and Remote Sensing, 49, 3249–3272, https://doi.org/10.1109/TGRS.2011.2158438, 2011.

Brodzik, M. J., Billingsley, B., Haran, T., Raup, B., and Savoie, M. H.: EASE-Grid 2.0: Incremental but Significant Improvements for Earth-Gridded Data Sets, ISPRS International Journal of Geo-Information, 1, 32–45, https://doi.org/10.3390/ijgi1010032, 2012.

Buehler, S. A., Jiménez, C., Evans, K. F., Eriksson, P., Rydberg, B., Heymsfield, A. J., Stubenrauch, C. J., Lohmann, U., Emde, C., John, V. O., Sreerekha, T. R., and Davis, C. P.: A concept for a satellite mission to measure cloud ice water path, ice particle size, and cloud altitude, Quarterly Journal of the Royal Meteorological Society, 133, 109–128, https://doi.org/10.1002/qj.143, 2007.

Cox, G. F. N. and Weeks, W. F.: Salinity Variations in Sea Ice, Journal of Glaciology, 13, 109–120, https://doi.org/10.3189/S0022143000023418, 1974.

Crameri, F.: Scientific colour maps, http://doi.org/10.5281/zenodo.1243862, 2018.

Crewell, S. and Löhnert, U.: Accuracy of cloud liquid water path from ground-based microwave radiometry 2. Sensor accuracy and synergy, Radio Science, 38, 8042, https://doi.org/10.1029/2002RS002634, 2003.

Crewell, S., Ebell, K., Löhnert, U., and Turner, D. D.: Can liquid water profiles be retrieved from passive microwave zenith observations?, Geophysical Research Letters, 36, 2008GL036 934, https://doi.org/10.1029/2008GL036934, 2009.

De Boer, G., Eloranta, E. W., and Shupe, M. D.: Arctic Mixed-Phase Stratiform Cloud Properties from Multiple Years of Surface-Based Measurements at Two High-Latitude Locations, Journal of the Atmospheric Sciences, 66, 2874–2887, https://doi.org/10.1175/2009JAS3029.1, 2009.

Di Tomaso, E., Bormann, N., and English, S.: Assimilation of ATOVS radiances at ECMWF: third year EUMETSAT fellowship report, European Centre for Medium-Range Weather Forecasts, Research Report No. 29, 2013.

Domine, F., Taillandier, A., and Simpson, W. R.: A parameterization of the specific surface area of seasonal snow for field use and for models of snowpack evolution, Journal of Geophysical Research: Earth Surface, 112, 2006JF000 512, https://doi.org/10.1029/2006JF000512, 2007.

Dorff, H., Aubry, C., Ewald, F., Hirsch, L., Jansen, F., Konow, H., Mech, M., Ori, D., Ringel, M., Walbröl, A., Crewell, S., Ehrlich, A., Wendisch, M., and Ament, F.: Unified Airborne Active and Passive Microwave Measurements over Arctic Sea Ice and Ocean during the HALO-(AC)^3 Campaign in Spring 2022 (v2.7), https://doi.org/10.1594/PANGAEA.974108, 2024.

Ebell, K., Löhnert, U., Päschke, E., Orlandi, E., Schween, J. H., and Crewell, S.: A 1-D variational retrieval of temperature, humidity, and liquid cloud properties: Performance under idealized and real conditions, Journal of Geophysical Research: Atmospheres, 122, 1746–1766, https://doi.org/10.1002/2016JD025945, 2017.

Ebell, K., Nomokonova, T., Maturilli, M., and Ritter, C.: Radiative Effect of Clouds at Ny-Ålesund, Svalbard, as Inferred from Ground-Based Remote Sensing Observations, Journal of Applied Meteorology and Climatology, 59, 3–22, https://doi.org/10.1175/JAMC-D-19-0080.1, 2020.

Ehrlich, A., Crewell, S., Herber, A., Klingebiel, M., Lüpkes, C., Mech, M., Becker, S., Borrmann, S., Bozem, H., Buschmann, M., Clemen, H.-C., De La Torre Castro, E., Dorff, H., Dupuy, R., Eppers, O., Ewald, F., George, G., Giez, A., Grawe, S., Gourbeyre, C., Hartmann, J., Jäkel, E., Joppe, P., Jourdan, O., Jurányi, Z., Kirbus, B., Lucke, J., Luebke, A. E., Maahn, M., Maherndl, N., Mallaun, C., Mayer, J., Mertes, S., Mioche, G., Moser, M., Müller, H., Pörtge, V., Risse, N., Roberts, G., Rosenburg, S., Röttenbacher, J., Schäfer, M., Schaefer, J., Schäfler, A., Schirmacher, I., Schneider, J., Schnitt, S., Stratmann, F., Tatzelt, C., Voigt, C., Walbröl, A., Weber, A., Wetzel, B., Wirth, M., and Wendisch, M.: A comprehensive in-situ and remote sensing data set collected during the HALO–$(AC)^3$ aircraft campaign, https://doi.org/10.5194/essd-2024-281, 2024.

Elsaesser, G. S., O'Dell, C. W., Lebsock, M. D., Bennartz, R., Greenwald, T. J., and Wentz, F. J.: The Multisensor Advanced Climatology of Liquid Water Path (MAC-LWP), Journal of Climate, 30, 10 193–10 210, https://doi.org/10.1175/JCLI-D-16-0902.1, 2017.

Ewald, F., Kölling, T., Baumgartner, A., Zinner, T., and Mayer, B.: Design and characterization of specMACS, a multipurpose hyperspectral cloud and sky imager, Atmospheric Measurement Techniques, 9, 2015–2042, https://doi.org/10.5194/amt-9-2015-2016, 2016.

Ewald, F., Groß, S., Hagen, M., Hirsch, L., Delanoë, J., and Bauer-Pfundstein, M.: Calibration of a 35 GHz airborne cloud radar: lessons learned and intercomparisons with 94 GHz cloud radars, Atmospheric Measurement Techniques, 12, 1815–1839, https://doi.org/10.5194/amt-12-1815-2019, 2019.

Geer, A. J.: Joint estimation of sea ice and atmospheric state from microwave imagers in operational weather forecasting, Quarterly Journal of the Royal Meteorological Society, 150, 3796–3826, https://doi.org/10.1002/qj.4797, 2024.

George, G., Luebke, A. E., Klingebiel, M., Mech, M., and Ehrlich, A.: Dropsonde measurements from HALO and POLAR 5 during HALO-$(AC)^3$ in 2022, https://doi.org/10.1594/PANGAEA.968891, type: dataset bundled publication, 2024.

Greenwald, T. J., Stephens, G. L., Vonder Haar, T. H., and Jackson, D. L.: A physical retrieval of cloud liquid water over the global oceans using special sensor microwave/imager (SSM/I) observations, Journal of Geophysical Research: Atmospheres, 98, 18 471–18 488, https://doi.org/10.1029/93JD00339, 1993.

Guedj, S., Karbou, F., Rabier, F., and Bouchard, A.: Toward a Better Modeling of Surface Emissivity to Improve AMSU Data Assimilation Over Antarctica, IEEE Transactions on Geoscience and Remote Sensing, 48, 1976–1985, https://doi.org/10.1109/TGRS.2009.2036254, 2010.

Haggerty, J. A., Curry, J. A., and Liu, G.: Potential for estimating cloud liquid water path over sea ice from airborne passive microwave measurements, Journal of Geophysical Research: Atmospheres, 107, https://doi.org/10.1029/2001JD000585, 2002.

Harlow, R. C. and Essery, R.: Tundra Snow Emissivities at MHS Frequencies: MEMLS Validation Using Airborne Microwave Data Measured During CLPX-II, IEEE Transactions on Geoscience and Remote Sensing, 50, 4262–4278, https://doi.org/10.1109/TGRS.2012.2193132, 2012.

Harris, C. R., Millman, K. J., Van Der Walt, S. J., Gommers, R., Virtanen, P., Cournapeau, D., Wieser, E., Taylor, J., Berg, S., Smith, N. J., Kern, R., Picus, M., Hoyer, S., Van Kerkwijk, M. H., Brett, M., Haldane, A., Del Río, J. F., Wiebe, M., Peterson, P., Gérard-Marchant,

P., Sheppard, K., Reddy, T., Weckesser, W., Abbasi, H., Gohlke, C., and Oliphant, T. E.: Array programming with NumPy, Nature, 585, 357–362, https://doi.org/10.1038/s41586-020-2649-2, 2020.

Hersbach, H., Bell, B., Berrisford, P., Hirahara, S., Horányi, A., Muñoz-Sabater, J., Nicolas, J., Peubey, C., Radu, R., Schepers, D., Simmons, A., Soci, C., Abdalla, S., Abellan, X., Balsamo, G., Bechtold, P., Biavati, G., Bidlot, J., Bonavita, M., De Chiara, G., Dahlgren, P., Dee, D., Diamantakis, M., Dragani, R., Flemming, J., Forbes, R., Fuentes, M., Geer, A., Haimberger, L., Healy, S., Hogan, R. J., Hólm, E., Janisková, M., Keeley, S., Laloyaux, P., Lopez, P., Lupu, C., Radnoti, G., de Rosnay, P., Rozum, I., Vamborg, F., Villaume, S., and Thépaut, J.-N.: Complete ERA5 from 1940: Fifth generation of ECMWF atmospheric reanalyses of the global climate, https://doi.org/10.24381/cds.143582cf, 2017.

Hersbach, H., Bell, B., Berrisford, P., Hirahara, S., Horányi, A., Muñoz-Sabater, J., Nicolas, J., Peubey, C., Radu, R., Schepers, D., Simmons, A., Soci, C., Abdalla, S., Abellan, X., Balsamo, G., Bechtold, P., Biavati, G., Bidlot, J., Bonavita, M., Chiara, G., Dahlgren, P., Dee, D., Diamantakis, M., Dragani, R., Flemming, J., Forbes, R., Fuentes, M., Geer, A., Haimberger, L., Healy, S., Hogan, R. J., Hólm, E., Janisková, M., Keeley, S., Laloyaux, P., Lopez, P., Lupu, C., Radnoti, G., Rosnay, P., Rozum, I., Vamborg, F., Villaume, S., and Thépaut, J.: The ERA5 global reanalysis, Quarterly Journal of the Royal Meteorological Society, 146, 1999–2049, https://doi.org/10.1002/qj.3803, 2020.

Hersbach, H., Bell, B., Berrisford, P., Biavati, G., Horányi, A., Muñoz Sabater, J., Nicolas, J., Peubey, C., Radu, R., Rozum, I., Schepers, D., Simmons, A., Soci, C., Dee, D., and Thépaut, J.-N.: ERA5 hourly data on pressure levels from 1940 to present, https://doi.org/10.24381/cds.bd0915c6, 2023.

Hewison, T. and English, S.: Airborne retrievals of snow and ice surface emissivity at millimeter wavelengths, IEEE Transactions on Geoscience and Remote Sensing, 37, 1871–1879, https://doi.org/10.1109/36.774700, 1999.

Hirahara, Y., Rosnay, P. d., and Arduini, G.: Evaluation of a Microwave Emissivity Module for Snow Covered Area with CMEM in the ECMWF Integrated Forecasting System, Remote Sensing, 12, 2946, https://doi.org/10.3390/rs12182946, 2020.

Hoyer, S. and Hamman, J.: xarray: N-D labeled Arrays and Datasets in Python, Journal of Open Research Software, 5, 10, https://doi.org/10.5334/jors.148, 2017.

Hunter, J. D.: Matplotlib: A 2D Graphics Environment, Computing in Science & Engineering, 9, 90–95, https://doi.org/10.1109/MCSE.2007.55, 2007.

Høyer, J. L., Lang, A. M., Eastwood, S., Wimmer, W., and Dybkj, G.: Report from Field Inter- Comparison Experiment (FICE) for ice surface temperature, Tech. rep., Danish Meteorological Institute, 2017.

Jacob, M., Ament, F., Gutleben, M., Konow, H., Mech, M., Wirth, M., and Crewell, S.: Investigating the liquid water path over the tropical Atlantic with synergistic airborne measurements, Atmospheric Measurement Techniques, 12, 3237–3254, https://doi.org/10.5194/amt-12-3237-2019, 2019.

Kalesse-Los, H., Schimmel, W., Luke, E., and Seifert, P.: Evaluating cloud liquid detection against Cloudnet using cloud radar Doppler spectra in a pre-trained artificial neural network, Atmospheric Measurement Techniques, 15, 279–295, https://doi.org/10.5194/amt-15-279-2022, 2022.

Kang, E., Sohn, B., Tonboe, R. T., Noh, Y., Kwon, I., Kim, S., Maturilli, M., Kim, H., and Liu, C.: Explicitly determined sea ice emissivity and emission temperature over the Arctic for surface-sensitive microwave channels, Quarterly Journal of the Royal Meteorological Society, 149, 2011–2030, https://doi.org/10.1002/qj.4492, 2023.

King, J., Howell, S., Brady, M., Toose, P., Derksen, C., Haas, C., and Beckers, J.: Local-scale variability of snow density on Arctic sea ice, The Cryosphere, 14, 4323–4339, https://doi.org/10.5194/tc-14-4323-2020, 2020.

Kneifel, S., Maahn, M., Peters, G., and Simmer, C.: Observation of snowfall with a low-power FM-CW K-band radar (Micro Rain Radar), Meteorology and Atmospheric Physics, 113, 75–87, https://doi.org/10.1007/s00703-011-0142-z, 2011.

Kneifel, S., Redl, S., Orlandi, E., Löhnert, U., Cadeddu, M. P., Turner, D. D., and Chen, M.-T.: Absorption Properties of Supercooled Liquid Water between 31 and 225 GHz: Evaluation of Absorption Models Using Ground-Based Observations, Journal of Applied Meteorology and Climatology, 53, 1028–1045, https://doi.org/10.1175/JAMC-D-13-0214.1, 2014.

Konow, H., Jacob, M., Ament, F., Crewell, S., Ewald, F., Hagen, M., Hirsch, L., Jansen, F., Mech, M., and Stevens, B.: A unified data set of airborne cloud remote sensing using the HALO Microwave Package (HAMP), Earth System Science Data, 11, 921–934, https://doi.org/10.5194/essd-11-921-2019, 2019.

Kunkee, D. B., Poe, G. A., Boucher, D. J., Swadley, S. D., Hong, Y., Wessel, J. E., and Uliana, E. A.: Design and Evaluation of the First Special Sensor Microwave Imager/Sounder, IEEE Transactions on Geoscience and Remote Sensing, 46, 863–883, https://doi.org/10.1109/TGRS.2008.917980, 2008.

Lawrence, H., Bormann, N., Sandu, I., Day, J., Farnan, J., and Bauer, P.: Use and impact of Arctic observations in the ECMWF Numerical Weather Prediction system, Quarterly Journal of the Royal Meteorological Society, 145, 3432–3454, https://doi.org/10.1002/qj.3628, 2019.

Luke, E. P., Kollias, P., and Shupe, M. D.: Detection of supercooled liquid in mixed-phase clouds using radar Doppler spectra, Journal of Geophysical Research: Atmospheres, 115, 2009JD012 884, https://doi.org/10.1029/2009JD012884, 2010.

Maahn, M., Turner, D. D., Löhnert, U., Posselt, D. J., Ebell, K., Mace, G. G., and Comstock, J. M.: Optimal Estimation Retrievals and Their Uncertainties: What Every Atmospheric Scientist Should Know, Bulletin of the American Meteorological Society, 101, E1512–E1523, https://doi.org/10.1175/BAMS-D-19-0027.1, 2020.

Maherndl, N., Moser, M., Lucke, J., Mech, M., Risse, N., Schirmacher, I., and Maahn, M.: Quantifying riming from airborne data during the HALO-$(AC)^3$ campaign, Atmospheric Measurement Techniques, 17, 1475–1495, https://doi.org/10.5194/amt-17-1475-2024, 2024.

McKinney, W.: Data Structures for Statistical Computing in Python, in: Proceedings of the 9th Python in Science Conference, pp. 56–61, Austin, Texas, https://doi.org/10.25080/Majora-92bf1922-00a, 2010.

Mech, M., Orlandi, E., Crewell, S., Ament, F., Hirsch, L., Hagen, M., Peters, G., and Stevens, B.: HAMP – the microwave package on the High Altitude and LOng range research aircraft (HALO), Atmospheric Measurement Techniques, 7, 4539–4553, https://doi.org/10.5194/amt-7-4539-2014, 2014.

Mech, M., Maahn, M., Kneifel, S., Ori, D., Orlandi, E., Kollias, P., Schemann, V., and Crewell, S.: PAMTRA 1.0: the Passive and Active Microwave radiative TRAnsfer tool for simulating radiometer and radar measurements of the cloudy atmosphere, Geoscientific Model Development, 13, 4229–4251, https://doi.org/10.5194/gmd-13-4229-2020, 2020.

Mech, M., Risse, N., Marrollo, G., and Paul, D.: ac3airborne, https://doi.org/10.5281/zenodo.7305586, 2022.

Merkouriadi, I., Gallet, J., Graham, R. M., Liston, G. E., Polashenski, C., Rösel, A., and Gerland, S.: Winter snow conditions on Arctic sea ice north of Svalbard during the Norwegian young sea ICE (N-ICE2015) expedition, Journal of Geophysical Research: Atmospheres, 122, https://doi.org/10.1002/2017JD026753, 2017.

Mätzler, C.: Relation between grain-size and correlation length of snow, Journal of Glaciology, 48, 461–466, https://doi.org/10.3189/172756502781831287, 2002.

Müller, J., Schäfer, M., Rosenburg, S., Ehrlich, A., and Wendisch, M.: Aerial maps of Arctic surface skin temperature and surface type during the HALO-$(AC)^3$ campaign in March/April 2022, https://doi.org/10.1594/PANGAEA.974454, artwork Size: 28 data points Pages: 28 data points, 2025a.

Müller, J. J., Schäfer, M., Rosenburg, S., Ehrlich, A., and Wendisch, M.: High-resolution maps of Arctic surface skin temperature and type retrieved from airborne thermal infrared imagery collected during the HALO-$(AC)^3$ campaign, https://doi.org/10.5194/amt-2024-3967, 2025b.

NASA Goddard Space Flight Center and GPM Intercalibration Working Group: NASA Global Precipitation Measurement (GPM) Level 1C Algorithms, Tech. Rep. GPM L1C ATBD (Version 1.9), Goddard Space Flight Center, Greenbelt, Maryland, USA, https://arthurhou.pps.eosdis.nasa.gov/Documents/L1C_ATBD_v1.9_GPMV07.pdf, 2022.

O'Dell, C. W., Wentz, F. J., and Bennartz, R.: Cloud Liquid Water Path from Satellite-Based Passive Microwave Observations: A New Climatology over the Global Oceans, Journal of Climate, 21, 1721–1739, https://doi.org/10.1175/2007JCLI1958.1, 2008.

Perro, C., Duck, T. J., Lesins, G., Strong, K., and Drummond, J. R.: Arctic Surface Properties and Their Impact on Microwave Satellite Water Vapor Column Retrievals, IEEE Transactions on Geoscience and Remote Sensing, 58, 8332–8344, https://doi.org/10.1109/TGRS.2020.2986302, 2020.

Picard, G., Brucker, L., Roy, A., Dupont, F., Fily, M., Royer, A., and Harlow, C.: Simulation of the microwave emission of multi-layered snowpacks using the Dense Media Radiative transfer theory: the DMRT-ML model, Geoscientific Model Development, 6, 1061–1078, https://doi.org/10.5194/gmd-6-1061-2013, 2013.

Picard, G., Sandells, M., and Löwe, H.: SMRT: an active–passive microwave radiative transfer model for snow with multiple microstructure and scattering formulations (v1.0), Geoscientific Model Development, 11, 2763–2788, https://doi.org/10.5194/gmd-11-2763-2018, 2018.

Prigent, C., Rossow, W. B., and Matthews, E.: Microwave land surface emissivities estimated from SSM/I observations, Journal of Geophysical Research, 102, 21 867–21 890, https://doi.org/10.1029/97JD01360, 1997.

Prigent, C., Aires, F., and Rossow, W. B.: Retrieval of Surface and Atmospheric Geophysical Variables over Snow-Covered Land from Combined Microwave and Infrared Satellite Observations, Journal of Applied Meteorology, 42, 368–380, https://doi.org/10.1175/1520-0450(2003)042<0368:ROSAAG>2.0.CO;2, 2003.

Rabe, B. and Geibert, W.: The Expedition PS144 of the Research Vessel POLARSTERN to the Arctic Ocean in 2024, https://doi.org/10.57738/BzPM_0794_2025, pages: 1–312 Place: Bremerhaven Publication Title: Berichte zur Polar- und Meeresforschung = Reports on polar and marine research Volume: 794, 2025.

Rantanen, M., Karpechko, A. Y., Lipponen, A., Nordling, K., Hyvärinen, O., Ruosteenoja, K., Vihma, T., and Laaksonen, A.: The Arctic has warmed nearly four times faster than the globe since 1979, Communications Earth & Environment, 3, 168, https://doi.org/10.1038/s43247-022-00498-3, 2022.

Risse, N.: Data related to: Cloud liquid water path detectability and retrieval accuracy from airborne passive microwave observations over Arctic sea ice, https://doi.org/10.5281/zenodo.15848709, 2025.

Risse, N.: nrisse/si-clouds: Code related to: Cloud liquid water path detectability and retrieval accuracy from airborne passive microwave observations over Arctic sea ice, https://doi.org/10.5281/zenodo.18237101, 2026.

Risse, N., Mech, M., Prigent, C., Spreen, G., and Crewell, S.: Assessing sea ice microwave emissivity up to submillimeter waves from airborne and satellite observations, The Cryosphere, 18, 4137–4163, https://doi.org/10.5194/tc-18-4137-2024, 2024.

Rodgers, C. D.: Inverse Methods for Atmospheric Sounding: Theory and Practice, vol. 2 of *Series on Atmospheric, Oceanic and Planetary Physics*, World Scientific, Singapore; River Edge, NJ, ISBN 981-281-371-3, 2000.

Rosenkranz, P. W.: Water vapor microwave continuum absorption: A comparison of measurements and models, Radio Science, 33, 919–928, https://doi.org/10.1029/98RS01182, 1998.

Rostosky, P., Spreen, G., Gerland, S., Huntemann, M., and Mech, M.: Modeling the Microwave Emission of Snow on Arctic Sea Ice for Estimating the Uncertainty of Satellite Retrievals, Journal of Geophysical Research: Oceans, 125, https://doi.org/10.1029/2019JC015465, 2020.

Rückert, J., Rostosky, P., Huntemann, M., Clemens-Sewall, D., Ebell, K., Kaleschke, L., Lemmetyinen, J., Macfarlane, A., Naderpour, R., Stroeve, J., Walbröl, A., and Spreen, G.: Sea ice concentration satellite retrievals influenced by surface changes due to warm air intrusions: A case study from the MOSAiC expedition., preprint, Oceanography and Atmospheric Sciences and Meteorology, https://doi.org/10.31223/X5VW85, 2023a.

Rückert, J. E., Huntemann, M., Tonboe, R. T., and Spreen, G.: Modeling Snow and Ice Microwave Emissions in the Arctic for a Multi-Parameter Retrieval of Surface and Atmospheric Variables From Microwave Radiometer Satellite Data, Earth and Space Science, 10, e2023EA003 177, https://doi.org/10.1029/2023EA003177, 2023b.

Rückert, J. E., Walbröl, A., Risse, N., Krobot, P., Haseneder-Lind, R., Mech, M., Ebell, K., and Spreen, G.: Microwave sea ice and ocean brightness temperature and emissivity between 22 and 243 GHz from ship-based radiometers, Annals of Glaciology, 66, e8, https://doi.org/10.1017/aog.2025.1, 2025.

Sandells, M., Lowe, H., Picard, G., Dumont, M., Essery, R., Floury, N., Kontu, A., Lemmetyinen, J., Maslanka, W., Morin, S., Wiesmann, A., and Matzler, C.: X-Ray Tomography-Based Microstructure Representation in the Snow Microwave Radiative Transfer Model, IEEE Transactions on Geoscience and Remote Sensing, 60, 1–15, https://doi.org/10.1109/TGRS.2021.3086412, 2022.

Sandells, M., Rutter, N., Wivell, K., Essery, R., Fox, S., Harlow, C., Picard, G., Roy, A., Royer, A., and Toose, P.: Simulation of Arctic snow microwave emission in surface-sensitive atmosphere channels, The Cryosphere, 18, 3971–3990, https://doi.org/10.5194/tc-18-3971-2024, 2024.

Schäfer, M., Wolf, K., Ehrlich, A., Hallbauer, C., Jäkel, E., Jansen, F., Luebke, A. E., Müller, J., Thoböll, J., Röschenthaler, T., Stevens, B., and Wendisch, M.: VELOX – a new thermal infrared imager for airborne remote sensing of cloud and surface properties, Atmospheric Measurement Techniques, 15, 1491–1509, https://doi.org/10.5194/amt-15-1491-2022, 2022.

Schäfer, M., Rosenburg, S., Ehrlich, A., Röttenbacher, J., and Wendisch, M.: Two-dimensional cloud-top and surface brightness temperature at spectral band BT3 (10.74 +/- 0.39 μm) with 1 Hz temporal resolution derived at flight altitude from VELOX during the HALO-(AC)^3 field campaign, https://doi.org/10.1594/PANGAEA.963382, 2023a.

Schäfer, M., Rosenburg, S., Ehrlich, A., Röttenbacher, J., and Wendisch, M.: Two-dimensional cloud-top and surface brightness temperature with 1 Hz temporal resolution derived at flight altitude from VELOX during the HALO-(AC)^3 field campaign, https://doi.org/10.1594/PANGAEA.963401, type: dataset publication series, 2023b.

Schäfer, M., Rosenburg, S., Ehrlich, A., Röttenbacher, J., and Wendisch, M.: One-dimensional cloud-top or surface brightness temperature with 20 Hz temporal resolution derived at flight altitude from VELOX-KT19 during the HALO-(AC)^3 field campaign, https://doi.org/10.1594/PANGAEA.967378, 2024.

Shupe, M. D.: A ground-based multisensor cloud phase classifier, Geophysical Research Letters, 34, 2007GL031 008, https://doi.org/10.1029/2007GL031008, 2007.

Shupe, M. D. and Intrieri, J. M.: Cloud Radiative Forcing of the Arctic Surface: The Influence of Cloud Properties, Surface Albedo, and Solar Zenith Angle, Journal of Climate, 17, 616–628, https://doi.org/10.1175/1520-0442(2004)017<0616:CRFOTA>2.0.CO;2, 2004.

Sledd, A., Shupe, M. D., Solomon, A., and Cox, C. J.: Surface Energy Balance Responses to Radiative Forcing in the Central Arctic From MOSAiC and Models, Journal of Geophysical Research: Atmospheres, 130, e2024JD042 578, https://doi.org/10.1029/2024JD042578, 2025.

Soriot, C., Picard, G., Prigent, C., Frappart, F., and Domine, F.: Year-round sea ice and snow characterization from combined passive and active microwave observations and radiative transfer modeling, Remote Sensing of Environment, 278, 113 061, https://doi.org/10.1016/j.rse.2022.113061, 2022.

Spreen, G., Kaleschke, L., and Heygster, G.: Sea ice remote sensing using AMSR-E 89-GHz channels, Journal of Geophysical Research, 113, C02S03, https://doi.org/10.1029/2005JC003384, 2008.

Stevens, B., Ament, F., Bony, S., Crewell, S., Ewald, F., Gross, S., Hansen, A., Hirsch, L., Jacob, M., Kölling, T., Konow, H., Mayer, B., Wendisch, M., Wirth, M., Wolf, K., Bakan, S., Bauer-Pfundstein, M., Brueck, M., Delanoë, J., Ehrlich, A., Farrell, D., Forde, M., Gödde, F., Grob, H., Hagen, M., Jäkel, E., Jansen, F., Klepp, C., Klingebiel, M., Mech, M., Peters, G., Rapp, M., Wing, A. A., and Zinner, T.: A High-Altitude Long-Range Aircraft Configured as a Cloud Observatory: The NARVAL Expeditions, Bulletin of the American Meteorological Society, 100, 1061–1077, https://doi.org/10.1175/BAMS-D-18-0198.1, 2019.

Stroeve, J., Nandan, V., Willatt, R., Dadic, R., Rostosky, P., Gallagher, M., Mallett, R., Barrett, A., Hendricks, S., Tonboe, R., McCrystall, M., Serreze, M., Thielke, L., Spreen, G., Newman, T., Yackel, J., Ricker, R., Tsamados, M., Macfarlane, A., Hannula, H.-R., and Schneebeli, M.: Rain on snow (ROS) understudied in sea ice remote sensing: a multi-sensor analysis of ROS during MOSAiC (Multidisciplinary drifting Observatory for the Study of Arctic Climate), The Cryosphere, 16, 4223–4250, https://doi.org/10.5194/tc-16-4223-2022, 2022.

Tan, I., Sotiropoulou, G., Taylor, P. C., Zamora, L., and Wendisch, M.: A Review of the Factors Influencing Arctic Mixed-Phase Clouds: Progress and Outlook, https://doi.org/10.1002/essoar.10508308.1, 2021.

Thielke, L., Huntemann, M., Hendricks, S., Jutila, A., Ricker, R., and Spreen, G.: Sea ice surface temperatures from helicopter-borne thermal infrared imaging during the MOSAiC expedition, Scientific Data, 9, 364, https://doi.org/10.1038/s41597-022-01461-9, 2022.

Timco, G. and Frederking, R.: A review of sea ice density, Cold Regions Science and Technology, 24, 1–6, https://doi.org/10.1016/0165-232X(95)00007-X, 1996.

Tonboe, R. T., Heygster, G., Pedersen, L. T., and Andersen, S.: Sea ice emission modelling, in: Thermal Microwave Radiation: Applications for Remote Sensing, edited by Mätzler, C., Electromagnetic Waves, pp. 382–400, Institution of Engineering and Technology, 2006.

Turner, D., Cadeddu, M., Lohnert, U., Crewell, S., and Vogelmann, A.: Modifications to the Water Vapor Continuum in the Microwave Suggested by Ground-Based 150-GHz Observations, IEEE Transactions on Geoscience and Remote Sensing, 47, 3326–3337, https://doi.org/10.1109/TGRS.2009.2022262, 2009.

Turner, D. D., Vogelmann, A. M., Austin, R. T., Barnard, J. C., Cady-Pereira, K., Chiu, J. C., Clough, S. A., Flynn, C., Khaiyer, M. M., Liljegren, J., Johnson, K., Lin, B., Long, C., Marshak, A., Matrosov, S. Y., McFarlane, S. A., Miller, M., Min, Q., Minimis, P., O'Hirok, W., Wang, Z., and Wiscombe, W.: Thin Liquid Water Clouds: Their Importance and Our Challenge, Bulletin of the American Meteorological Society, 88, 177–190, https://doi.org/10.1175/BAMS-88-2-177, 2007.

Turner, D. D., Kneifel, S., and Cadeddu, M. P.: An Improved Liquid Water Absorption Model at Microwave Frequencies for Supercooled Liquid Water Clouds, Journal of Atmospheric and Oceanic Technology, 33, 33–44, https://doi.org/10.1175/JTECH-D-15-0074.1, 2016.

UK Met Office: Cartopy: A cartographic python library with Matplotlib support, http://scitools.org.uk/cartopy/docs/latest/, 2023.

Vargel, C., Royer, A., St-Jean-Rondeau, O., Picard, G., Roy, A., Sasseville, V., and Langlois, A.: Arctic and subarctic snow microstructure analysis for microwave brightness temperature simulations, Remote Sensing of Environment, 242, 111 754, https://doi.org/10.1016/j.rse.2020.111754, 2020.

Virtanen, P., Gommers, R., Oliphant, T. E., Haberland, M., Reddy, T., Cournapeau, D., Burovski, E., Peterson, P., Weckesser, W., Bright, J., Van Der Walt, S. J., Brett, M., Wilson, J., Millman, K. J., Mayorov, N., Nelson, A. R. J., Jones, E., Kern, R., Larson, E., Carey, C. J., Polat, I., Feng, Y., Moore, E. W., VanderPlas, J., Laxalde, D., Perktold, J., Cimrman, R., Henriksen, I., Quintero, E. A., Harris, C. R., Archibald,

A. M., Ribeiro, A. H., Pedregosa, F., Van Mulbregt, P., SciPy 1.0 Contributors, Vijaykumar, A., Bardelli, A. P., Rothberg, A., Hilboll, A., Kloeckner, A., Scopatz, A., Lee, A., Rokem, A., Woods, C. N., Fulton, C., Masson, C., Häggström, C., Fitzgerald, C., Nicholson, D. A., Hagen, D. R., Pasechnik, D. V., Olivetti, E., Martin, E., Wieser, E., Silva, F., Lenders, F., Wilhelm, F., Young, G., Price, G. A., Ingold, G.-L., Allen, G. E., Lee, G. R., Audren, H., Probst, I., Dietrich, J. P., Silterra, J., Webber, J. T., Slavič, J., Nothman, J., Buchner, J., Kulick, J., Schönberger, J. L., De Miranda Cardoso, J. V., Reimer, J., Harrington, J., Rodríguez, J. L. C., Nunez-Iglesias, J., Kuczynski, J., Tritz, K., Thoma, M., Newville, M., Kümmerer, M., Bolingbroke, M., Tartre, M., Pak, M., Smith, N. J., Nowaczyk, N., Shebanov, N., Pavlyk, O., Brodtkorb, P. A., Lee, P., McGibbon, R. T., Feldbauer, R., Lewis, S., Tygier, S., Sievert, S., Vigna, S., Peterson, S., More, S., Pudlik, T., Oshima, T., Pingel, T. J., Robitaille, T. P., Spura, T., Jones, T. R., Cera, T., Leslie, T., Zito, T., Krauss, T., Upadhyay, U., Halchenko, Y. O., and Vázquez-Baeza, Y.: SciPy 1.0: fundamental algorithms for scientific computing in Python, Nature Methods, 17, 261–272, https://doi.org/10.1038/s41592-019-0686-2, 2020.

Voss, S., Heygster, G., and Ezraty, R.: Improving sea ice type discrimination by the simultaneous use of SSM/I and scatterometer data, Polar Research, 22, 35–42, 2003.

Vuyovich, C. M., Jacobs, J. M., Hiemstra, C. A., and Deeb, E. J.: Effect of spatial variability of wet snow on modeled and observed microwave emissions, Remote Sensing of Environment, 198, 310–320, https://doi.org/10.1016/j.rse.2017.06.016, 2017.

Walbröl, A., Crewell, S., Engelmann, R., Orlandi, E., Griesche, H., Radenz, M., Hofer, J., Althausen, D., Maturilli, M., and Ebell, K.: Atmospheric temperature, water vapour and liquid water path from two microwave radiometers during MOSAiC, Scientific Data, 9, 534, https://doi.org/10.1038/s41597-022-01504-1, 2022.

Walbröl, A., Michaelis, J., Becker, S., Dorff, H., Ebell, K., Gorodetskaya, I., Heinold, B., Kirbus, B., Lauer, M., Maherndl, N., Maturilli, M., Mayer, J., Müller, H., Neggers, R. A. J., Paulus, F. M., Röttenbacher, J., Rückert, J. E., Schirmacher, I., Slättberg, N., Ehrlich, A., Wendisch, M., and Crewell, S.: Contrasting extremely warm and long-lasting cold air anomalies in the North Atlantic sector of the Arctic during the HALO-$(AC)^3$ campaign, Atmospheric Chemistry and Physics, 24, 8007–8029, https://doi.org/10.5194/acp-24-8007-2024, 2024.

Wang, D., Prigent, C., Kilic, L., Fox, S., Harlow, C., Jimenez, C., Aires, F., Grassotti, C., and Karbou, F.: Surface Emissivity at Microwaves to Millimeter Waves over Polar Regions: Parameterization and Evaluation with Aircraft Experiments, Journal of Atmospheric and Oceanic Technology, 34, 1039–1059, https://doi.org/10.1175/JTECH-D-16-0188.1, 2017.

Warren, S. G., Rigor, I. G., Untersteiner, N., Radionov, V. F., Bryazgin, N. N., Aleksandrov, Y. I., and Colony, R.: Snow Depth on Arctic Sea Ice, Journal of Climate, 12, 1814–1829, https://doi.org/10.1175/1520-0442(1999)012<1814:SDOASI>2.0.CO;2, 1999.

Waskom, M.: seaborn: statistical data visualization, https://doi.org/10.5281/zenodo.4645478, 2021.

Weber, A., Kölling, T., Pörtge, V., Baumgartner, A., Rammeloo, C., Zinner, T., and Mayer, B.: Polarization upgrade of specMACS: calibration and characterization of the 2D RGB polarization-resolving cameras, Atmospheric Measurement Techniques, 17, 1419–1439, https://doi.org/10.5194/amt-17-1419-2024, 2024a.

Weber, A., Pörtge, V., Zinner, T., and Mayer, B.: Spectral radiance measurements with the hyperspectral and polarized imaging system specMACS during the HALO-$(AC)^3$ field campaign, https://doi.org/10.1594/PANGAEA.966992, 2024b.

Wendisch, M., Crewell, S., Ehrlich, A., Herber, A., Kirbus, B., Lüpkes, C., Mech, M., Abel, S. J., Akansu, E. F., Ament, F., Aubry, C., Becker, S., Borrmann, S., Bozem, H., Brückner, M., Clemen, H.-C., Dahlke, S., Dekoutsidis, G., Delanoë, J., De La Torre Castro, E., Dorff, H., Dupuy, R., Eppers, O., Ewald, F., George, G., Gorodetskaya, I. V., Grawe, S., Groß, S., Hartmann, J., Henning, S., Hirsch, L., Jäkel, E., Joppe, P., Jourdan, O., Jurányi, Z., Karalis, M., Kellermann, M., Klingebiel, M., Lonardi, M., Lucke, J., Luebke, A., Maahn, M., Maherndl, N., Maturilli, M., Mayer, B., Mayer, J., Mertes, S., Michaelis, J., Michalkov, M., Mioche, G., Moser, M., Müller, H., Neggers, R., Ori, D., Paul, D., Paulus, F., Pilz, C., Pithan, F., Pöhlker, M., Pörtge, V., Ringel, M., Risse, N., Roberts, G. C., Rosenburg, S., Röttenbacher,

J., Rückert, J., Schäfer, M., Schäfer, J., Schemannn, V., Schirmacher, I., Schmidt, J., Schmidt, S., Schneider, J., Schnitt, S., Schwarz, A., Siebert, H., Sodemann, H., Sperzel, T., Spreen, G., Stevens, B., Stratmann, F., Svensson, G., Tatzelt, C., Tuch, T., Vihma, T., Voigt, C., Volkmer, L., Walbröl, A., Weber, A., Wehner, B., Wetzel, B., Wirth, M., and Zinner, T.: Overview: Quasi-Lagrangian observations of Arctic air mass transformations – Introduction and initial results of the HALO–(AC)^3 aircraft campaign, https://doi.org/10.5194/egusphere-2024-783, 2024.

Westwater, E. R., Han, Y., Shupe, M. D., and Matrosov, S. Y.: Analysis of integrated cloud liquid and precipitable water vapor retrievals from microwave radiometers during the Surface Heat Budget of the Arctic Ocean project, Journal of Geophysical Research: Atmospheres, 106, 32 019–32 030, https://doi.org/10.1029/2000JD000055, 2001.

Wiesmann, A. and Mätzler, C.: Microwave Emission Model of Layered Snowpacks, Remote Sensing of Environment, 70, 307–316, https://doi.org/10.1016/S0034-4257(99)00046-2, 1999.

Wiesmann, A., Mätzler, C., and Weise, T.: Radiometric and structural measurements of snow samples, Radio Science, 33, 273–289, https://doi.org/10.1029/97RS02746, 1998.

Wirth, M. and Groß, S.: Aircraft measurements of backscatter ratio, particle depolarization and water vapour molecular density profiles over Arctic sea ice and ocean during the HALO-(AC)^3 campaign in spring 2022, https://doi.org/10.1594/PANGAEA.967086, 2024.

Wirth, M., Fix, A., Mahnke, P., Schwarzer, H., Schrandt, F., and Ehret, G.: The airborne multi-wavelength water vapor differential absorption lidar WALES: system design and performance, Applied Physics B, 96, 201–213, https://doi.org/10.1007/s00340-009-3365-7, 2009.

Wivell, K., Fox, S., Sandells, M., Harlow, C., Essery, R., and Rutter, N.: Evaluating Snow Microwave Radiative Transfer (SMRT) model emissivities with 89 to 243 GHz observations of Arctic tundra snow, The Cryosphere, 17, 4325–4341, https://doi.org/10.5194/tc-17-4325-2023, 2023.